

Implicit Neural Compression of Point Clouds

Hongning Ruan, Yulin Shao, Qianqian Yang, Liang Zhao, Zhaoyang Zhang, Dusit Niyato

Abstract—Point clouds have gained prominence in numerous applications due to their ability to accurately depict 3D objects and scenes. However, compressing unstructured, high-precision point cloud data effectively remains a significant challenge. In this paper, we propose NeRC³, a novel point cloud compression framework leveraging implicit neural representations to handle both geometry and attributes. Our approach employs two coordinate-based neural networks to implicitly represent a voxelized point cloud: the first determines the occupancy status of a voxel, while the second predicts the attributes of occupied voxels. By feeding voxel coordinates into these networks, the receiver can efficiently reconstruct the original point cloud’s geometry and attributes. The neural network parameters are quantized and compressed alongside auxiliary information required for reconstruction. Additionally, we extend our method to dynamic point cloud compression with techniques to reduce temporal redundancy, including a 4D spatial-temporal representation termed 4D-NeRC³. Experimental results validate the effectiveness of our approach: for static point clouds, NeRC³ outperforms octree-based methods in the latest G-PCC standard. For dynamic point clouds, 4D-NeRC³ demonstrates superior geometry compression compared to state-of-the-art G-PCC and V-PCC standards and achieves competitive results for joint geometry and attribute compression.

Index Terms—Point cloud compression, implicit neural representation, neural network compression.

I. INTRODUCTION

Point clouds have become a widely used format for representing 3D objects and scenes across diverse applications such as autonomous driving, augmented reality/virtual reality (AR/VR), digital twins, and robotics [1]–[3]. Fundamentally, a point cloud consists of a collection of 3D points distributed throughout volumetric space, each characterized by its spatial coordinates. These coordinates can be quantized into integer values, resulting in the formation of voxels in 3D space, similar to pixels in 2D images – a process known as voxelization. Beyond geometric data, each point typically carries additional attributes such as color, normal vectors, and reflectance. Recent advancements in sensing technologies have enabled the capture of large-scale point clouds with high-resolution spatial and attribute information. Furthermore, real-world objects and dynamic scenes are often captured over time, producing sequences known as dynamic point clouds. However, the vast data volume, sparse distribution, and unstructured nature of raw point clouds demand substantial memory for storage or

high bandwidth for transmission, highlighting the pressing need for efficient point cloud compression (PCC) [1], [4].

The Moving Picture Experts Group (MPEG) initiated the standardization of PCC in 2017, which culminated in 2020 with the establishment of two primary approaches: video-based PCC (V-PCC) and geometry-based PCC (G-PCC) [1]. V-PCC is specifically tailored for compressing dynamic point clouds, while G-PCC focuses on static point clouds or dynamically captured LiDAR sequences. Both standards rely on conventional representations of point cloud data, such as octrees, triangle meshes, and 3D-to-2D projections. Inspired by the success of learned image compression, recent research has explored the potential of deep learning for PCC [2], [5]–[12]. These methods often employ autoencoder architectures, where encoders transform input point clouds into latent representations and decoders reconstruct the original input data. While such learning-based methods exhibit performance gains over traditional approaches, they typically require large point cloud datasets for network training. Moreover, as highlighted in [13], the performance of these networks on unseen test data is significantly influenced by the choice of training datasets.

In recent years, deep neural networks (DNNs) have been employed to implicitly represent 3D objects and scenes by learning continuous functions that take spatial coordinates as inputs and produce corresponding features. This approach, known as implicit neural representations (INRs), has found applications across various research areas, including 3D shape modeling [14], [15], differentiable rendering [16], and image/video compression [17]–[20]. INRs provide a promising new direction for PCC, as demonstrated by several existing studies [21]–[23]. However, most of these works primarily focus on either the geometry or the attributes of point clouds. In contrast, the use of INRs for compressing dynamic point clouds remains an area with limited exploration.

Contributions: In this paper, we present a novel framework for compressing both the geometry and attributes of a single point cloud, named implicit Neural Representations for Colored point Cloud Compression (NeRC³). Drawing inspiration from INRs for 3D shapes, our approach utilizes two coordinate-based DNNs to implicitly represent voxelized point clouds. The first network predicts whether a given voxel is occupied or unoccupied based on its spatial coordinates, outputting an occupancy probability (OP). To efficiently handle the typically sparse nature of 3D space, we partition the space into smaller cubes and focus only on voxels within non-empty cubes as network inputs. After computing the occupancy probability, a threshold is applied to determine binary occupancy, enabling the reconstruction of the original point cloud geometry by identifying occupied voxels. The second network predicts attributes for these occupied voxels, taking spatial coordinates as input and producing correspond-

H. Ruan, Q. Yang, L. Zhao and Z. Zhang are with the Department of Information Science and Electronic Engineering, Zhejiang University (e-mails: {rhoehning, qianqianyang20, lzhaol2020, ning_ming}@zju.edu.cn).

Y. Shao is with the State Key Laboratory of Internet of Things for Smart City and the Department of Electrical and Computer Engineering, University of Macau, Macau S.A.R. (e-mail: ylshao@um.edu.mo).

D. Niyato is with the School of Computer Science and Engineering, Nanyang Technological University, Singapore (e-mail: dnyato@ntu.edu.cn)

ing attribute values. To encode a point cloud, we fit these two networks specifically to the given data, then quantize and encode their parameters, alongside auxiliary information such as non-empty cubes and the occupancy threshold. During decoding, the parameters are retrieved, and the two DNNs are used to reconstruct the point cloud’s geometry and attributes, respectively.

For dynamic PCC, our proposed method can be applied directly as an intra-frame compression technique, compressing each frame individually. This approach is referred to as i-NeRC³. To further minimize temporal redundancy across frames, we extend our method with several additional strategies. The first approach involves residual compression of network parameters between successive frames, leveraging the assumption that these parameters exhibit high similarity. The second approach connects the optima of networks across frames using a trained Bezier curve in latent neural space, encoding the curve rather than the individual network parameters it connects. This assumes that the curve is relatively simple and requires significantly fewer bits for encoding. These two techniques, termed r-NeRC³ and c-NeRC³, respectively, aim to exploit the temporal correlations of network parameters. Additionally, we propose 4D spatial-temporal representations (4D-NeRC³) for dynamic point clouds, which directly address redundancy in the point cloud space by treating a sequence of point clouds as a single 4D structure, represented implicitly by two DNNs.

Experimental results demonstrate the effectiveness of our proposed methods. In static PCC, NeRC³ achieves significant performance improvements over octree-based algorithms employed by the latest G-PCC standard, with a BD-BR gain of 70.39% for geometry compression and 26.58% for joint geometry and attribute compression. For dynamic PCC, 4D-NeRC³ effectively reduces temporal redundancy, outperforming octree-based G-PCC by 89.07% and 71.05% BD-BR gains for compression with and without attributes, respectively. Furthermore, it surpasses G-PCC (trisoup) and the latest V-PCC standard in geometry compression, while achieving comparable performance for joint geometry and attribute compression.

Organization: The remainder of this paper is organized as follows. Section II provides a review of existing studies on PCC and INRs. Our proposed PCC framework is detailed in Section III, with an extension to dynamic PCC described in Section IV. Experimental results are presented in Section V. Section VI concludes this paper. For the reader’s convenience, frequently used notations throughout the paper are summarized in Table I.

II. RELATED WORKS

This section overviews several relevant works, covering PCC standards and techniques, as well as the various applications of INRs.

A. Standardization

The MPEG 3D Graphics Coding Group has established standards for PCC to address the growing need for efficient data representation and storage. Two distinct approaches have

TABLE I: Notations.

Notation	Description
N	Bit depth of voxels
M	Bit depth of cubes
T	Frame group size
$P = n + 1$	Number of control points
α, β	Sampling ratios ($\alpha + \beta = 1$)
λ_F, λ_G	Regularization strengths
Δ_F, Δ_G	Quantization step sizes
\mathcal{X}	Point cloud geometry ^{1,2,3}
$C(\cdot) : \mathcal{X} \rightarrow [0, 1]^3$	Point cloud attributes ^{1,2,3}
$\mathcal{T} = \{0, 1, \dots, T - 1\}$	Frame indices
$\mathcal{S} = \{0, 1, \dots, 2^N - 1\}^3$	Voxels in 3D space
$\mathcal{S}_{\text{local}} = \{0, 1, \dots, 2^{N-M} - 1\}^3$	Local coordinates in a single cube
\mathcal{W}	Non-empty cubes ^{1,3}
\mathcal{V}	Voxels in non-empty cubes ^{1,3}
$F(\cdot) : \mathcal{V} \rightarrow [0, 1]$	Network for geometry ³
$G(\cdot) : \hat{\mathcal{X}} \rightarrow [0, 1]^3$	Network for attributes ³
Θ, Φ	Network parameters ^{1,2,3}
$p(\cdot)$	Occupancy probability of a voxel ²
$y(\cdot)$	Ground-truth occupancy of a voxel
$\mathbf{c}_{\text{predicted}}(\cdot)$	Predicted color of a voxel ²
$\mathbf{c}_{\text{expected}}(\cdot)$	Expected color of a voxel
$D_F(\cdot), D_G(\cdot)$	Voxel-wise distortion
$\mathcal{P}_F, \mathcal{P}_G$	Distribution of training samples
$\mathcal{L}_F(\cdot), \mathcal{L}_G(\cdot)$	Training loss
τ	Threshold ¹

¹ A superscript $(\cdot)^{(t)}$ can be used to specify the frame index.

² A hat $\widehat{(\cdot)}$ can be used to indicate that the notation is the lossy version at the decoder.

³ An overline $\overline{(\cdot)}$ can be used to extend the notation to 4D representations.

been introduced [1]: V-PCC for the compression of dynamic point clouds, and G-PCC for static point clouds and dynamically captured LiDAR sequences.

V-PCC operates by transforming 3D point cloud data into 2D projections, making it particularly suitable for dense point clouds with smooth surfaces. The process begins by dividing the point cloud into connected regions, known as 3D patches, which are independently projected into 2D patches and arranged in 2D images. These images can then be efficiently compressed using established image/video codecs, such as HEVC [24]. In contrast, G-PCC directly encodes geometry and attributes in 3D space. For geometry compression, G-PCC uses an octree structure to represent voxelized point cloud geometry. The process involves partitioning the volume into eight sub-cubes and recursively dividing occupied cubes. Each node in the octree carries a binary label indicating whether a cube is occupied, forming a binary string that is compressed using entropy coding. Additionally, G-PCC offers a geometry coding technique called triangle soup (trisoup), which approximates object surfaces using triangle meshes and performs particularly well at low bit rates. For attribute compression, G-PCC employs linear transforms based on geometry, including the region-adaptive hierarchical transform (RAHT) [25], which predicts attribute values at higher levels of the octree based on lower-level values. G-PCC further enhances its performance with improved entropy coding and prediction of RAHT coefficients.

B. Learned PCC

End-to-end learned compression approaches have demonstrated superior rate-distortion performance compared to traditional methods in image compression [26]–[30]. Inspired by these advances, a range of works have explored the application of deep learning to PCC. These methods predominantly leverage the autoencoder architecture, wherein the encoder transforms an input point cloud into latent features, and the decoder reconstructs the original input. To optimize rate-distortion performance, an entropy model is integrated and acts as a prior on the latent features. Additionally, hyperprior models have been introduced to enhance the accuracy of probability estimation during the encoding of latent features. Given that point clouds lack the structured nature of images, diverse network architectures have been developed for PCC. For instance, [2], [5], [7] utilize 3D dense or sparse convolutional autoencoders to represent voxelized point cloud geometry. Similarly, [8], [9] apply 3D sparse convolutions to compress point cloud attributes. In contrast to these voxel-based methods, [10], [11] employ PointNet-style architectures to directly compress raw points instead of converting them into voxel grids.

Recently, deep learning techniques have also been applied to dynamic PCC. Studies such as [31]–[33] employ 3D sparse convolutions to perform inter-frame prediction within the feature space, subsequently compressing the feature residuals. In contrast, [34] introduces a point-based compression module that leverages inter-frame correlations to compress point-wise features. However, these approaches are primarily limited to geometry compression, leaving the compression of attributes largely unaddressed.

C. Implicit Neural Representations

Implicit neural representations, a.k.a. neural fields, have emerged as a powerful method for representing various types of data, including audio signals, images, and volumetric content. This approach utilizes a neural network to map spatial or temporal coordinates to their corresponding features, with each network typically overfitted to a specific data instance. For instance, the geometry of 3D shapes can be represented implicitly using fully-connected neural networks, a.k.a. multilayer perceptrons (MLPs), which learn either signed distance functions (SDF) [35], [36] or occupancy functions [14], [15], [37]. INRs have also found applications in differentiable rendering, where 3D scenes are reconstructed from 2D images. A notable example is the neural radiance field (NeRF) [16], which fits a single neural network to a large collection of images from a single 3D scene, enabling photo-realistic synthesis of novel views.

Thanks to their highly efficient representational capabilities, INRs have found applications in image and video compression. For instance, [17]–[19] utilize neural networks to represent images by mapping pixel coordinates to corresponding RGB values, a technique known as pixel-wise representation, followed by quantization and encoding of the network parameters. In contrast, [20] introduces an innovative image-wise representation for video compression, where a combination of

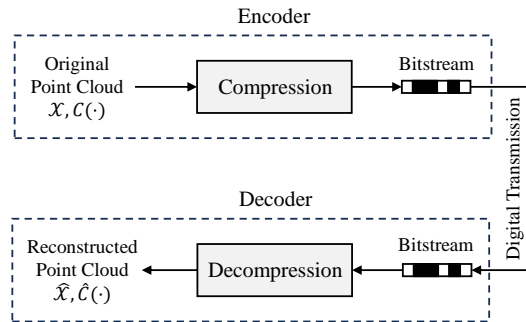


Fig. 1: Block diagram of a PCC system. The encoder compresses the original point cloud into a bitstream for digital transmission. The decoder receives this bitstream and reconstructs a lossy version of the point cloud through decompression.

an MLP and convolutional networks generates entire frames using only the frame index as input. Departing from pixel- or frame-wise methods, [38] takes a different approach by assigning each frame group its own network, which takes patch coordinates as input and produces patch volumes for the group.

The application of INRs in image/video compression and 3D shape modeling has laid the groundwork for INR-based PCC. While this is a relatively new field, a few notable works exist. For example, [21] trains a convolutional neural network alongside input latent codes, where each latent code is used by the network to reconstruct the occupancies of points within a local region. This method encodes the network and all latent codes as representations of point cloud geometry; however, it diverges from our definition of INRs as it does not use coordinates as inputs to the network. In contrast, [23] employs a single coordinate-based neural network to generate point cloud attributes, while [22] similarly predicts attributes using a coordinate-based network, enhanced with input latent vectors as local parameters. Additionally, [39] focuses on encoding LiDAR point cloud sequences by first projecting the LiDAR data into a 2D range image sequence and subsequently applying INR-based image/video compression.

It is important to distinguish between INR-based PCC and scene compression. A 3D scene is typically represented as a collection of images captured from different viewpoints. Inspired by neural rendering techniques, some works [40], [41] train neural fields to implicitly represent scenes and subsequently compress the parameters of these fields. At the receiver’s end, neural fields are used for rendering the scene. It is worth noting that in scene compression, both the original and retrieved data consist of images, and the neural fields themselves do not construct 3D content. Similarly, [42] introduces a method for representing 3D dynamic content as a sequence of Neural Radiance Fields (NeRF). While the original paper applies this approach to dynamic PCC, we still categorize it as scene compression since it generates only images, without constructing point clouds.

III. INR-BASED POINT CLOUD COMPRESSION

This section begins by formulating the problem of PCC, providing a clear context for the challenges addressed by

our approach. We then offer an overview of our proposed framework, followed by an in-depth discussion of its key components. For now, we concentrate on the compression of static point clouds, with the exploration of dynamic PCC deferred to Section IV.

A. Problem Formulation

A point cloud is a collection of 3D points in the volumetric space, with each point defined by its spatial coordinates. We assume that the point cloud is voxelized with an N -bit resolution, i.e., the coordinates of all points are quantized into N -bit integers. This voxelization process generates $2^N \times 2^N \times 2^N$ voxels within the volumetric space, each represented by coordinate $\mathbf{x} \in \{0, 1, \dots, 2^N - 1\}^3$. We denote the entire space after voxelization as

$$\mathcal{S} = \{0, 1, \dots, 2^N - 1\}^3. \quad (1)$$

Additionally, each point may be associated with corresponding attributes. In this work, we consider RGB colors as the attributes of points, where the RGB components range from 0 to 1.

The block diagram of a PCC system is shown in Fig. 1. We use $\{\mathcal{X}, \mathcal{C}\}$ to denote the original point cloud, where \mathcal{X} contains the coordinates of all points, representing the geometry, and $\mathcal{C}(\cdot)$ maps each point $\mathbf{x} \in \mathcal{X}$ to its corresponding attributes $\mathcal{C}(\mathbf{x})$. The encoder transforms the original point cloud into a bitstream through the compression process. These bits are transmitted to the decoder through digital transmission. The decoder receives these bits, and reconstructs a lossy version of the point cloud, denoted by $\{\hat{\mathcal{X}}, \hat{\mathcal{C}}\}$, through the decompression process, where $\hat{\mathcal{X}}$ contains the reconstructed points, and $\hat{\mathcal{C}}(\cdot)$ maps each reconstructed point $\hat{\mathbf{x}} \in \hat{\mathcal{X}}$ to its lossy attributes $\hat{\mathcal{C}}(\hat{\mathbf{x}})$.

In this work, we address two scenarios of PCC. The first scenario focuses on geometry compression, where only the spatial structure of the point cloud is considered, neglecting associated attribute data. The second scenario involves joint compression of both geometry and attributes, targeting colored point clouds, which compresses both the geometric structure and its associated attributes simultaneously.

For geometry compression, we use point-to-point error (D1) in peak signal-to-noise ratio (PSNR) to quantify the geometry distortion, following MPEG PCC common test conditions [43]. Formally, the point-to-point error of a point cloud \mathcal{B} relative to a reference point cloud \mathcal{A} is defined as

$$e(\mathcal{B}, \mathcal{A}) = \frac{1}{|\mathcal{B}|} \sum_{\mathbf{b} \in \mathcal{B}} \min_{\mathbf{a} \in \mathcal{A}} \|\mathbf{b} - \mathbf{a}\|_2^2. \quad (2)$$

The error is calculated in two directions, yielding $e(\mathcal{B}, \mathcal{A})$ and $e(\mathcal{A}, \mathcal{B})$. After that, the D1 PSNR between \mathcal{B} and \mathcal{A} is given by

$$\text{D1 PSNR} = 10 \log_{10} \frac{3 \times (2^N - 1)^2}{\max\{e(\mathcal{B}, \mathcal{A}), e(\mathcal{A}, \mathcal{B})\}} \text{(dB)}. \quad (3)$$

For joint compression of both geometry and attributes, we use PCQM [44], a full-reference quality metric for colored 3D point clouds, as our evaluation metric. This metric quantifies

the overall distortion of both geometry and attributes, aligning more closely with the human visual system.

The compressed bit rate is measured by bits per point (bpp), i.e., the total number of bits divided by the number of points in the original point cloud.

B. Compression Pipeline

As shown in Fig. 2, to compress a point cloud, we first implicitly represent the point cloud with neural networks, followed by quantization and encoding of network parameters. These quantized parameters, along with some auxiliary information, are then used at the decoder to reconstruct a lossy version of the original point cloud. The detailed operations within our NeRC³ framework are elaborated below.

1) *Pre-Processing*: As stated above, the entire volumetric space comprises $2^N \times 2^N \times 2^N$ voxels, and reconstructing the point cloud requires determining whether each voxel is occupied by a point or remains empty. However, the vast number of voxels in the space presents a challenge, as a considerable portion of these voxels are typically empty, making the processing of all voxels highly inefficient and time-consuming. To mitigate this issue, we divide the space into $2^M \times 2^M \times 2^M$ cubes, with each cube containing $2^{N-M} \times 2^{N-M} \times 2^{N-M}$ voxels. The location of each cube is represented by a coordinate $\mathbf{w} \in \{0, 1, \dots, 2^M - 1\}^3$. For any given voxel \mathbf{x} , the cube containing it is identified by $\mathbf{w} = \lfloor \mathbf{x} / 2^{N-M} \rfloor$, where $\lfloor \cdot \rfloor$ denotes the floor function. The set of coordinates representing all non-empty cubes is denoted by \mathcal{W} , expressed as

$$\mathcal{W} = \{\mathbf{w} : \mathbf{w} = \lfloor \mathbf{x} / 2^{N-M} \rfloor, \mathbf{x} \in \mathcal{X}\}. \quad (4)$$

Since the voxels outside these cubes are empty, we only consider voxels within these cubes, the set of which is denoted by

$$\mathcal{V} = \{\mathbf{x} : \lfloor \mathbf{x} / 2^{N-M} \rfloor \in \mathcal{W}, \mathbf{x} \in \mathcal{S}\}. \quad (5)$$

When selecting the value of M , there is a trade-off between the size of \mathcal{W} and \mathcal{V} . For the decoder to know which cubes are non-empty, \mathcal{W} should be encoded as auxiliary information and transmitted to the decoder. Therefore, we choose M to ensure that \mathcal{W} only takes up a small proportion of the encoded bits. This may lead to a large size of \mathcal{V} , which requires significant memory for storage, especially for a high-resolution point cloud. Nevertheless, \mathcal{V} is a stack of cubes and thus has a regular and hierarchical structure. Hence, voxels in \mathcal{V} can be accessed in a more elegant way without storing all these voxels in advance. We denote the set containing all local coordinates inside a cube as

$$\mathcal{S}_{\text{local}} = \{0, 1, \dots, 2^{N-M} - 1\}^3. \quad (6)$$

To sample a voxel from \mathcal{V} , we first sample a cube \mathbf{w} from \mathcal{W} and then sample the local coordinate $\mathbf{x}_{\text{local}}$ from $\mathcal{S}_{\text{local}}$, where the latter can be generated as random numbers. Then the global coordinate can be expressed as $\mathbf{x} = \mathbf{x}_{\text{local}} + 2^{N-M} \mathbf{w}$. Similarly, to loop over the voxels in \mathcal{V} , we first loop over the cubes in \mathcal{W} , and then enumerate the local coordinates for each cube.

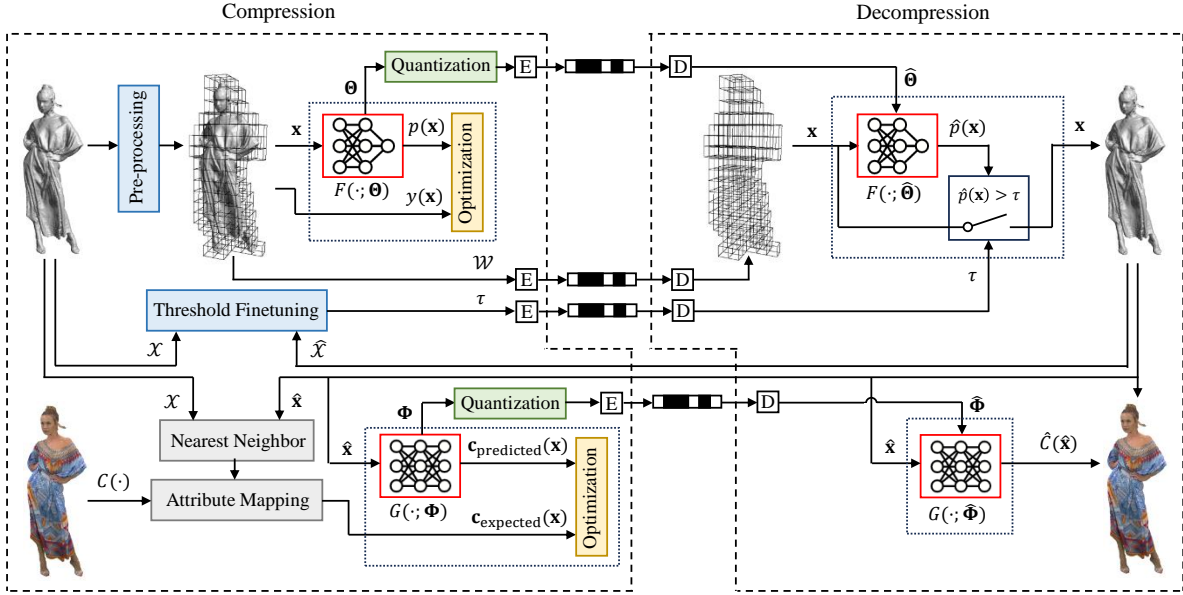


Fig. 2: Overview of our NeRC³ framework. The encoder optimizes two neural networks, F and G , to implicitly represent the geometry and attributes respectively, followed by quantization and encoding of network parameters, Θ and Φ . They are transmitted to the decoder along with some auxiliary information, i.e., non-empty cubes \mathcal{W} and the threshold τ . The decoder can reconstruct a lossy version of the original point cloud using quantized network parameters and the auxiliary information. “E” and “D” denote lossless encoding and decoding, respectively. The arrows from “Decompression” pointing back to “Compression” mean that the encoder performs the decompression process to obtain the lossy point cloud, which may be used in the following steps of compression.

2) *Geometry Compression*: We employ a neural network F , parameterized by Θ , to represent the geometry of the original point cloud by classifying each voxel as occupied or not. The network takes the coordinate \mathbf{x} as input and outputs a single real number between 0 and 1. As mentioned before, we only consider voxels in \mathcal{V} as inputs to the network. The output value can be seen as the occupancy probability (OP):

$$p(\mathbf{x}) = F(\mathbf{x}; \Theta). \quad (7)$$

When training F , we optimize the network parameters to ensure that the output probability $p(\mathbf{x})$ is close to the ground-truth occupancy $y(\mathbf{x})$. We label the occupied voxels as 1 and empty ones as 0. Thus, the occupancy can be expressed by the indicator function $\mathbb{I}(\cdot)$ as

$$y(\mathbf{x}) = \mathbb{I}(\mathbf{x} \in \mathcal{X}) = \begin{cases} 1, & \mathbf{x} \in \mathcal{X}, \\ 0, & \mathbf{x} \notin \mathcal{X}. \end{cases} \quad (8)$$

The network parameters serve as an implicit representation of the point cloud geometry. They are first quantized, followed by lossless entropy coding, and then transmitted to the decoder. Therefore, the decoder can only retrieve the quantized version of parameters. For a given step size Δ_F , the quantized parameters can be formulated as

$$\hat{\Theta} = \lfloor \Theta / \Delta_F \rfloor \cdot \Delta_F, \quad (9)$$

where $\lfloor \cdot \rfloor$ represents the rounding operation. We denote the OP obtained using quantized parameters as $\hat{p}(\mathbf{x}) = F(\mathbf{x}; \hat{\Theta})$. After obtaining $\hat{p}(\mathbf{x})$, a threshold τ is chosen to determine the binary occupancy. Specifically, the decoder interprets each input voxel as occupied if its OP $\hat{p}(\mathbf{x})$ exceeds the threshold

τ , and empty otherwise. All occupied voxels in the non-empty cubes are aggregated to form the reconstructed geometry:

$$\hat{\mathcal{X}} = \{\mathbf{x} : F(\mathbf{x}; \hat{\Theta}) > \tau, \mathbf{x} \in \mathcal{V}\}. \quad (10)$$

In addition to the parameters $\hat{\Theta}$, reconstructing geometry also requires the input voxels \mathcal{V} and the threshold τ , where \mathcal{V} can be determined by \mathcal{W} . Hence, we encode \mathcal{W} and τ as auxiliary information. They are transmitted together with $\hat{\Theta}$ to constitute the complete representation of geometry.

3) *Attribute Compression*: Before attribute compression, the encoder first performs compression and decompression on the geometry, and leverage the reconstructed geometry $\hat{\mathcal{X}}$ as prior knowledge. We utilize another neural network G , parameterized by Φ , to represent the attributes of the point cloud. The network takes an occupied voxel $\hat{\mathbf{x}}$ from the reconstructed geometry as input, and generates its RGB color as output, represented by $\mathbf{c}_{\text{predicted}}(\hat{\mathbf{x}})$.

$$\mathbf{c}_{\text{predicted}}(\hat{\mathbf{x}}) = G(\hat{\mathbf{x}}; \Phi). \quad (11)$$

In the training process of G , we optimize the network parameters to ensure that the predicted color for each input voxel is close to its expected color. Because the reconstructed geometry $\hat{\mathcal{X}}$ may differ from the ground-truth geometry \mathcal{X} , to minimize the overall distortion, we define the color of each voxel as the ground-truth color of its nearest neighbor in the original point cloud, formulated as

$$\mathbf{c}_{\text{expected}}(\hat{\mathbf{x}}) = C \left(\arg \min_{\mathbf{x} \in \mathcal{X}} \|\mathbf{x} - \hat{\mathbf{x}}\|_2^2 \right). \quad (12)$$

Similar to the geometry compression, the neural field parameters have to be quantized using a given step size Δ_G . The

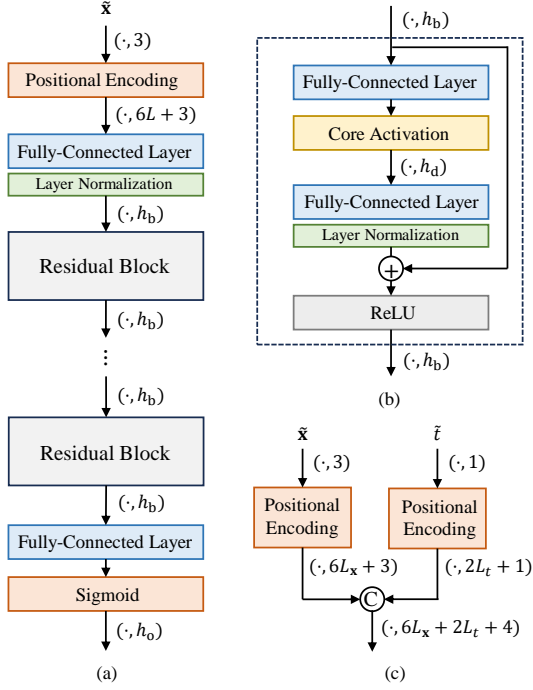


Fig. 3: (a) The network structure, which contains multiple residual blocks. (b) The detailed structure of each residual block. We use ReLU as the core activation for F , and use the sine activation for G . The plus sign “+” denotes residual connection. (c) Separate positional encoding for the spatial and temporal coordinates. “C” denotes concatenation. Please refer to Section. IV-C for details.

decoder only retrieves the quantized parameters $\hat{\Phi}$, expressed as

$$\hat{\Phi} = \lfloor \Phi / \Delta_G \rfloor \cdot \Delta_G. \quad (13)$$

The reconstruction of attributes is much simpler than reconstructing geometry. The coordinates of the occupied voxels in reconstructed geometry are fed into G to generate the corresponding attributes, with no auxiliary information needed.

$$\hat{C}(\hat{\mathbf{x}}) = G(\hat{\mathbf{x}}; \hat{\Phi}). \quad (14)$$

C. Network Details

1) *Network Structure*: Both F and G are coordinate-based fully-connected networks that take 3D vectors as inputs. The detailed structure of both networks is presented in Fig. 3(a)-(b). Each network contains multiple residual blocks [45] that take h_b -dimensional inputs and generate h_b -dimensional outputs. To match the dimensions, two additional fully-connected layers are placed at the input and output of the network separately. Each residual block consists of two fully-connected layers with h_d hidden channels. In addition, a core activation is placed in the middle of the two layers and a ReLU activation is at the output of the block. We use ReLU as the core activation for F , and use the sine activation [46] with a frequency ω_0 for G . Besides, we perform layer normalization on some layers in the network. For the last layer at the output, we use the sigmoid function to obtain output values in the range $[0, 1]$. The network F has an output dimension $h_o = 1$ while the output dimension for G is $h_o = 3$.

We apply positional encoding to map the input coordinate to a higher dimensional space using the encoding function as in [16]. The encoding function is defined as follows:

$$\Gamma(\tilde{\mathbf{x}}) = (\tilde{\mathbf{x}}, \sin(2^0 \pi \tilde{\mathbf{x}}), \cos(2^0 \pi \tilde{\mathbf{x}}), \dots, \sin(2^{L-1} \pi \tilde{\mathbf{x}}), \cos(2^{L-1} \pi \tilde{\mathbf{x}})), \quad (15)$$

where L determines the number of different frequencies. Before feeding the coordinate \mathbf{x} into the encoding function, they are first normalized to $[-1, 1]$. We denote the normalized coordinate by $\tilde{\mathbf{x}}$. The encoding function maps each coordinate component from a single scalar to a vector of length $(2L + 1)$, containing more high-frequency variations than the original input.

In our experiment, we set the input and output dimension of residual blocks as $h_b = 512$, and the hidden dimension as $h_d = 128$. The network F contains 2 residual blocks while the network G contains 3. We set $L = 12$ and $\omega_0 = 64$.

2) *Loss Function*: We optimize the two networks F, G by minimizing the following loss functions respectively:

$$\mathcal{L}_F(\Theta) = \mathbb{E}_{\mathbf{x} \sim \mathcal{P}_F} [D_F(\mathbf{x})] + \frac{\lambda_F}{|\mathcal{X}|} \|\Theta\|_1, \quad (16)$$

$$\mathcal{L}_G(\Phi) = \mathbb{E}_{\hat{\mathbf{x}} \sim \mathcal{P}_G} [D_G(\hat{\mathbf{x}})] + \frac{\lambda_G}{|\mathcal{X}|} \|\Phi\|_1, \quad (17)$$

where $D_F(\cdot), D_G(\cdot)$ denote the distortion loss of each voxel, and $\mathcal{P}_F, \mathcal{P}_G$ represent the distribution of training samples that will be discussed in the next subsection. The first term of each loss function is the expectation of voxel-wise distortion over the sampled voxels and the second term applies ℓ_1 -regularization to network parameters.

We adopt α -balanced focal loss [47] as the geometry distortion loss. The distortion of each voxel \mathbf{x} is defined as

$$D_F(\mathbf{x}) = -\tilde{\alpha}(\mathbf{x}) \cdot (1 - \tilde{p}(\mathbf{x}))^\gamma \log(\tilde{p}(\mathbf{x})), \quad (18)$$

where

$$\tilde{\alpha}(\mathbf{x}) = y(\mathbf{x}) \cdot \alpha + (1 - y(\mathbf{x})) \cdot (1 - \alpha), \quad (19)$$

$$\tilde{p}(\mathbf{x}) = y(\mathbf{x}) \cdot p(\mathbf{x}) + (1 - y(\mathbf{x})) \cdot (1 - p(\mathbf{x})), \quad (20)$$

$\alpha \in (0, 1)$ and $\gamma \geq 0$ are hyperparameters.

The focal loss is based on the traditional binary cross-entropy (BCE) loss. In addition to the original form of BCE, the focal loss uses a modulating factor $(1 - \tilde{p})^\gamma$ to introduce higher weights for misclassified voxels. Following [47], we set $\gamma = 2$. Besides, a weighting factor $\tilde{\alpha}$ is used to balance the two classes of voxels. The hyperparameter α can be set to the proportion of empty voxels.

We define the attribute distortion loss per voxel as the MSE of the predicted color and expected color:

$$D_G(\hat{\mathbf{x}}) = \|\mathbf{c}_{\text{predicted}}(\hat{\mathbf{x}}) - \mathbf{c}_{\text{expected}}(\hat{\mathbf{x}})\|_2^2. \quad (21)$$

Some existing works (e.g., [21], [22]) apply entropy models to estimate bit rates, and minimize rate-distortion loss functions during training. However, we empirically find that employing entropy models slows down and destabilizes the training process. Inspired by ℓ_1 -regularization, we incorporate the ℓ_1 norm of the original network parameters into our loss functions. As ℓ_1 -regularization pushes the network parameters

to zero, we can easily obtain sparse networks at low bit rates after entropy coding. Different bit rates can be achieved through adjusting the regularization strength λ_F and λ_G .

D. Sampling Strategy

The section investigates the sampling strategy of voxels for training, i.e., the distributions, \mathcal{P}_F and \mathcal{P}_G . For a better explanation, we define a notation to represent the distribution of uniform sampling. Formally, if \mathbf{a} is uniformly sampled from a given set \mathcal{A} , then $\mathbf{a} \sim \mathcal{U}(\mathcal{A})$, and the probability mass function (PMF) of \mathbf{a} is given by

$$\mathcal{U}(\mathbf{a}; \mathcal{A}) = \begin{cases} 1/|\mathcal{A}|, & \mathbf{a} \in \mathcal{A}, \\ 0, & \mathbf{a} \notin \mathcal{A}. \end{cases} \quad (22)$$

During training, a straightforward strategy is to uniformly sample voxels among all possible inputs of the network. For network F , the possible input voxels are within \mathcal{V} , thus $\mathcal{P}_F = \mathcal{U}(\mathcal{V})$. For network G , the input voxels are from the reconstructed geometry $\hat{\mathcal{X}}$, thus $\mathcal{P}_G = \mathcal{U}(\hat{\mathcal{X}})$. In our experiment, we adopt uniform sampling only for training G , with a more involved sampling strategy for training F , as elaborated below.

When training F , we manually control the ratio of the occupied voxels among training samples. We denote this ratio by a hyperparameter $\beta \in (0, 1)$. Recall that the focal loss uses a parameter α to balance the samples, where α is the proportion of the empty voxels, thus $\alpha = 1 - \beta$. Following this sampling strategy, we can sample voxels from the occupied space \mathcal{X} with probability β and from the empty space $\mathcal{V} - \mathcal{X}$ with probability α . Hence, the distribution of training samples is represented as

$$\mathcal{P}_F = \beta \cdot \mathcal{U}(\mathcal{X}) + \alpha \cdot \mathcal{U}(\mathcal{V} - \mathcal{X}), \quad (23)$$

which indicates that the PMF of an arbitrary voxel \mathbf{x} is $\mathcal{P}_F(\mathbf{x}) = \beta \cdot \mathcal{U}(\mathbf{x}; \mathcal{X}) + \alpha \cdot \mathcal{U}(\mathbf{x}; \mathcal{V} - \mathcal{X})$.

To uniformly sample voxels from the empty space $\mathcal{V} - \mathcal{X}$, we have to store all these empty voxels in advance. However, for a high-resolution point cloud, the empty space will become extremely large, and storing these voxels will consume much memory. Therefore, instead of sampling voxels from $\mathcal{V} - \mathcal{X}$, we uniformly sample voxels from \mathcal{V} . Recall that voxels in \mathcal{V} can be sampled in a hierarchical way. We uniformly sample a cube $\mathbf{w} \sim \mathcal{U}(\mathcal{W})$ and randomly generate the local coordinate $\mathbf{x}_{\text{local}} \sim \mathcal{U}(\mathcal{S}_{\text{local}})$. Then the corresponding global coordinate $\mathbf{x} = \mathbf{x}_{\text{local}} + 2^{N-M}\mathbf{w}$ can be regarded as uniformly sampled from \mathcal{V} , i.e., $\mathbf{x} \sim \mathcal{U}(\mathcal{V})$, because each voxel in \mathcal{V} is accessed with equal probabilities.

However, note that \mathcal{V} contains occupied voxels. If we still sample occupied voxels from \mathcal{X} with probability β , the overall ratio of occupied voxels in training samples will be greater than β . Therefore, we modify the above sampling strategy into the following expression, without changing the sample distribution:

$$\mathcal{P}_F = \beta^* \cdot \mathcal{U}(\mathcal{X}) + \alpha^* \cdot \mathcal{U}(\mathcal{V}), \quad (24)$$

where β^* and α^* are the adjusted sampling ratios, given by

$$\beta^* = \frac{\beta - \zeta}{1 - \zeta}, \quad \alpha^* = \frac{\alpha}{1 - \zeta}, \quad (25)$$

$$\zeta = \frac{|\mathcal{X}|}{|\mathcal{V}|} = \frac{|\mathcal{X}|}{(2^{N-M})^3 |\mathcal{W}|}. \quad (26)$$

As long as the ratio of occupied voxels in training samples is no less than the real proportion of occupied voxels in \mathcal{V} , i.e., $\beta \geq \zeta$, we can replace sampling from $\mathcal{V} - \mathcal{X}$ with sampling from \mathcal{V} , with a small adjustment on the sampling ratios. Since the real proportion ζ is usually very small, $\beta \geq \zeta$ can easily hold in practice.

E. Threshold Fine-tuning

Recall that we use a threshold τ to predict the occupancies of voxels in \mathcal{V} , as described in (10). The value of τ plays a critical role in the geometry reconstruction process, even after the network parameters are optimized and fixed. Consequently, the encoder must fine-tune this threshold to achieve optimal reconstruction quality, specifically by maximizing the D1 Peak Signal-to-Noise Ratio (PSNR) between the original point cloud \mathcal{X} and the reconstructed point cloud $\hat{\mathcal{X}}$. It is important to note that the decoder has access only to the quantized parameters. Therefore, to ensure consistent information between the encoder and decoder, quantization is manually applied to the parameters at the encoder before the threshold fine-tuning step.

We consider the D1 PSNR between \mathcal{X} and $\hat{\mathcal{X}}$ as a function of the threshold τ , denoted as $D(\tau)$. Consequently, the task of threshold fine-tuning can be formulated as finding the maximum point of the function $D(\tau)$. To gain deeper insights into the behavior and characteristics of this function, we propose and analyze several of its properties.

Proposition 1. *There exists a threshold boundary $\tau_{\text{max}} \in (0, 1)$ such that the following holds:*

- For $\tau \in [0, \tau_{\text{max}})$, $D(\tau)$ is piecewise constant and right-continuous.
- For $\tau \in [\tau_{\text{max}}, 1]$, $D(\tau)$ is undefined.

Proof. See Appendix A. ■

To introduce the next property, we define the distance between a point \mathbf{b} to a reference point cloud \mathcal{A} as the Euclidean distance from \mathbf{b} to its nearest neighbor within the set \mathcal{A} . This can be expressed mathematically as

$$d(\mathbf{b}, \mathcal{A}) = \min_{\mathbf{a} \in \mathcal{A}} \|\mathbf{b} - \mathbf{a}\|_2^2. \quad (27)$$

Proposition 2. *Let the following assumptions hold:*

- 1) $|\tilde{\mathcal{X}}_{\text{max}}| \leq |\mathcal{X}|$, where $\tilde{\mathcal{X}}_{\text{max}} = \{\mathbf{x} : \hat{p}(\mathbf{x}) = \tau_{\text{max}}, \mathbf{x} \in \mathcal{V}\}$ denotes the set of voxels with the maximum OP.
- 2) For any \mathbf{x}_0 , it satisfies $d(\mathbf{x}_0, \mathcal{X}) \geq \mathbb{E}_{\mathbf{x} \sim \mathcal{U}(\tilde{\mathcal{X}}_h(\mathbf{x}_0))} [d(\mathbf{x}, \mathcal{X})]$, where $\tilde{\mathcal{X}}_h(\mathbf{x}_0) = \{\mathbf{x} : \hat{p}(\mathbf{x}) > \hat{p}(\mathbf{x}_0), \mathbf{x} \in \mathcal{V}\}$ denotes the set of voxels with higher OPs than \mathbf{x}_0 .

Then, $D(\tau)$ is unimodal, meaning that there exists a value $\tau^ \in (0, \tau_{\text{max}})$ such that $D(\tau)$ is non-decreasing on $[0, \tau^*)$ and non-increasing on $(\tau^*, \tau_{\text{max}})$.*

Proof. See Appendix B. ■

Next, we analyze the practical implications of the above propositions within the context of experimental situations. Given that OPs are predicted by a neural network, it is highly

unlikely for the network to produce identical output values for different inputs. As such, it is reasonable to approximate the number of subintervals is approximately $|\mathcal{V}|$. In practice, however, it becomes challenging to perceive $D(\tau)$ as a piecewise constant function, as suggested in Proposition 1. This is due to the typically large size of $|\mathcal{V}|$, which results in each subinterval being exceedingly small and thus indistinguishable, making $D(\tau)$ appear more like a smooth and continuous function.

Regarding Proposition 2, the low likelihood of duplicate OPs means that assumption 1) generally holds without difficulty. In theory, assumption 2) could be substituted with a stronger and more intuitive condition: for any \mathbf{x}_0 and \mathbf{x}_1 , where \mathbf{x}_1 has a higher OP than \mathbf{x}_0 , it should hold that $d(\mathbf{x}_0, \mathcal{X}) \geq d(\mathbf{x}_1, \mathcal{X})$. This condition represents an ideal scenario for the distribution of voxel OPs. Since the network learns a continuous function fitted by ground-truth occupancy during training, voxels with higher OPs should theoretically be closer to the occupied voxels in \mathcal{X} , resulting in a smaller distance $d(\mathbf{x}, \mathcal{X})$. However, this condition is rarely satisfied in practice. For instance, OPs may exhibit fluctuations in empty regions, causing voxels with relatively higher OPs to be situated far from \mathcal{X} . The assumption 2) in Proposition 2 relaxes this requirement by only necessitating that the average distance of higher-OP voxels remains small, thereby tolerating outliers with larger distances. Our experimental results indicate that $D(\tau)$ can be well-approximated as a strictly unimodal function. Consequently, we identify its maximum using the golden section search, as detailed in Algorithm 1.

IV. INR-BASED DYNAMIC POINT CLOUD COMPRESSION

In this section, we address the problem of dynamic PCC, focusing on the compression of point cloud frame sequences. While NeRC³ can be directly applied as an intra-frame compression method, i.e., compressing each frame independently – an approach we refer to as i-NeRC³ – it does not effectively reduce temporal redundancy between frames. To overcome this limitation, we introduce several methods designed to exploit the temporal correlations across frames, thereby enhancing overall compression efficiency.

A. Residual Compression

To represent a point cloud sequence, we use a superscript $(\cdot)^{(t)}$ to specify the frame index, $t = 0, 1, 2, \dots$. For instance, the t -th point cloud frame is denoted by $\{\mathcal{X}^{(t)}, C^{(t)}\}$, the corresponding non-empty cubes are represented $\mathcal{W}^{(t)}$, and voxels within these cubes are represented by $\mathcal{V}^{(t)}$.

We first draw our inspiration from [42]. It represents each point cloud frame as a 3D scene using NeRF and has observed that the NeRF parameters of two successive frames share high similarity. Based on this observation, it encodes the parameter differences between consecutive frames instead of encoding each frame separately, resulting in lower bit rates. We incorporate this strategy into our NeRC³ framework and name it as r-NeRC³.

For brevity, we take geometry compression as an example where each frame is represented by a single neural network.

Algorithm 1 Threshold fine-tuning via golden section search.

Input: Original point cloud \mathcal{X} , quantized network parameters $\hat{\Theta}$, input voxels \mathcal{V} , number of iterations I
Output: Optimal threshold τ

- 1: $l \leftarrow 0$
- 2: $r \leftarrow 1$
- 3: $D_1 \leftarrow \text{None}$
- 4: $D_2 \leftarrow \text{None}$
- 5: **for** $i = 0$ to $I - 1$ **do**
- 6: $m_1 \leftarrow l + (3 - \sqrt{5})/2 \cdot (r - l)$
- 7: $m_2 \leftarrow l + (\sqrt{5} - 1)/2 \cdot (r - l)$
- 8: **if** $D_1 = \text{None}$ **then**
- 9: $\hat{\mathcal{X}} \leftarrow \{\mathbf{x} : F(\mathbf{x}; \hat{\Theta}) > m_1, \mathbf{x} \in \mathcal{V}\}$
- 10: **if** $\hat{\mathcal{X}} = \emptyset$ **then**
- 11: $D_1 \leftarrow -\infty$
- 12: **else**
- 13: $D_1 \leftarrow \text{D1 PSNR between } \hat{\mathcal{X}} \text{ and } \mathcal{X}$
- 14: **if** $D_2 = \text{None}$ **then**
- 15: $\hat{\mathcal{X}} \leftarrow \{\mathbf{x} : F(\mathbf{x}; \hat{\Theta}) > m_2, \mathbf{x} \in \mathcal{V}\}$
- 16: **if** $\hat{\mathcal{X}} = \emptyset$ **then**
- 17: $D_2 \leftarrow -\infty$
- 18: **else**
- 19: $D_2 \leftarrow \text{D1 PSNR between } \hat{\mathcal{X}} \text{ and } \mathcal{X}$
- 20: **if** $D_2 \neq -\infty$ and $D_1 < D_2$ **then**
- 21: $l \leftarrow m_1$
- 22: $D_1 \leftarrow D_2$
- 23: $D_2 \leftarrow \text{None}$
- 24: **else**
- 25: $r \leftarrow m_2$
- 26: $D_2 \leftarrow D_1$
- 27: $D_1 \leftarrow \text{None}$
- 28: $\tau \leftarrow (l + r)/2$
- 29: **return** τ

The attributes can be treated in the same manner. Let $\Theta^{(t)}$ denote the parameters of the t -th network representing the geometry of the t -th frame $\mathcal{X}^{(t)}$, $t = 0, 1, 2, \dots$. For the first frame, the encoder optimizes the parameters $\Theta^{(0)}$, performs quantization, and then transmits the quantized parameters $\hat{\Theta}^{(0)}$ to the decoder, as done in the previous section. For the remaining frames ($t = 1, 2, \dots$), the encoder still trains the complete parameters $\Theta^{(t)}$, but only quantizes and transmits the residual w.r.t. the previous frame, formulated by

$$\delta\Theta^{(t)} = \Theta^{(t)} - \hat{\Theta}^{(t-1)}, \quad (28)$$

$$\delta\hat{\Theta}^{(t)} = \lfloor \delta\Theta^{(t)} / \Delta_F \rfloor \cdot \Delta_F. \quad (29)$$

After receiving $\delta\hat{\Theta}^{(t)}$, the decoder retrieves the complete parameters by adding it to the buffered parameters for the previous frame:

$$\hat{\Theta}^{(t)} = \hat{\Theta}^{(t-1)} + \delta\hat{\Theta}^{(t)}. \quad (30)$$

Since the encoder only encodes the residual, we replace the ℓ_1 norm $\|\Theta^{(t)}\|_1$ in the loss function with $\|\delta\Theta^{(t)}\|_1 = \|\Theta^{(t)} - \hat{\Theta}^{(t-1)}\|_1$, where $\hat{\Theta}^{(t-1)}$ is frozen during the training process.

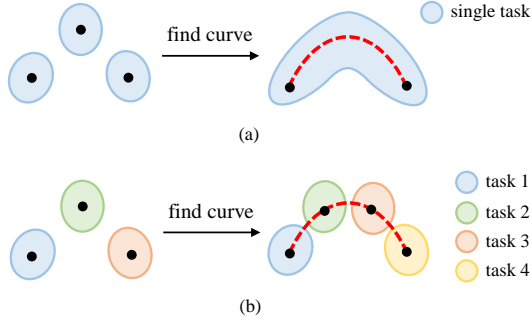


Fig. 4: Demonstration of the connectivity of optima in neural space, where the colored regions represent low-loss regions for different tasks. (a) A simple curve in one low-loss region connects the optima for a single task. (b) A simple curve running through the low-loss regions for different tasks connects the optima for these tasks sequentially.

Residual compression is expected to reduce temporal redundancy and thereby achieve bit rate savings. However, empirical results reveal that its performance is actually worse than compressing each frame individually, particularly for geometry compression. We attribute this to the following reasons. Unlike [42], which treats a point cloud as a 3D scene representation, our approach focuses on reconstructing point occupancies. Since these points are predominantly distributed on the surface of the scene, successive frames of the point cloud exhibit minimal similarity in terms of occupancy, leading to substantial differences between their network parameters.

B. Connectivity of Optima in Neural Space

Here, we propose another approach to reduce the temporal redundancy of network parameters. This approach, named as c-NeRC³, is inspired by previous works on mode connectivity [48], [49], which state that different optima of neural networks trained on the same task are connected by simple low-loss paths in neural space, such as polygonal chain and Bezier curve. We extend the connectivity of optima to a sequence of tasks, and use a single path to connect the optima of different tasks sequentially.

A visual demonstration is given in Fig. 4. Due to the continuity of loss functions, a given task is matched with a connected low-loss region in the neural space, and networks inside this region yield low loss values when evaluated by the corresponding loss function for this task.

- If there is only one task, as in Fig. 4(a), the optima of independently trained three networks are isolated in the plane. To find a curve that connects the optima, [49] first separately trains two networks that serve as the end points and then trains a simple curve to connect the two end points. The found curve is contained in a single low-loss region.
- If there are four different tasks, as in Fig. 4(b), the optima of independently trained networks for these tasks are not coplanar in neural space. Instead, we directly train a curve that runs through low-loss regions for these tasks. By appropriately sampling points on the curve, we can obtain

a point in each low-loss region, i.e., an optimal neural network for each task.

Take geometry compression as an example. For clarity, we rewrite some of the notations in the previous section. In the expression for geometry distortion, i.e., (18), the probability $p(\mathbf{x}) = F(\mathbf{x}; \Theta)$ is derived from network parameters Θ and the occupancy $y(\mathbf{x}) = \mathbb{I}(\mathbf{x} \in \mathcal{X})$ is determined by ground-truth geometry \mathcal{X} . Therefore, the distortion $D_F(\mathbf{x})$ is conditioned on Θ and \mathcal{X} . We rewrite the notation as $D_F(\mathbf{x}; \Theta, \mathcal{X})$ to specify the conditions, which means that the geometry distortion of voxel \mathbf{x} is calculated using Θ and \mathcal{X} . Similarly, the training sample distribution \mathcal{P}_F , i.e., (24), is conditioned on the original geometry \mathcal{X} , because voxels from \mathcal{X} and \mathcal{V} are sampled separately, where \mathcal{V} can be determined by \mathcal{X} . We use the notation $\mathcal{P}_F(\mathcal{X})$ to specify the condition. Besides, since we mainly focus on the connectivity of optima in neural space, with slight abuse of notation, this subsection uses the term ‘‘point’’ to refer to points in neural space, which is actually a parameter set of a neural network.

We segment a point cloud sequence into groups of size T , and encode each group as an independent sequence $\mathcal{X}^{(0)}, \mathcal{X}^{(1)}, \dots, \mathcal{X}^{(T-1)}$. For each group, we construct T tasks, where the t -th task is to represent $\mathcal{X}^{(t)}$ with a neural network parameterized by $\Theta^{(t)}$. The corresponding loss function for the t -th task is

$$\mathcal{L}_F^{(t)}(\Theta^{(t)}) = \mathbb{E}_{\mathbf{x} \sim \mathcal{P}_F(\mathcal{X}^{(t)})} [D_F(\mathbf{x}; \Theta^{(t)}, \mathcal{X}^{(t)})]. \quad (31)$$

Let $\mathbb{R}^{|\Theta|}$ denote the neural space, where $|\Theta|$ is the number of parameters of network F . We assume that $\Theta^{(0)}, \Theta^{(1)}, \dots, \Theta^{(T-1)}$ can be sampled with evenly spaced time parameters on a Bezier curve in the neural space. Formally, the t -th sample point can be expressed as

$$\Theta^{(t)} = \sum_{i=0}^n \binom{n}{i} \left(\frac{t}{T-1} \right)^i \left(1 - \frac{t}{T-1} \right)^{n-i} \Theta_i, \quad (32)$$

where $\Theta_0, \Theta_1, \dots, \Theta_n \in \mathbb{R}^{|\Theta|}$ represent the control points, and n denotes the degree of Bezier curve. We take the normalized frame index $t/(T-1) \in [0, 1]$ as the time parameter of the curve. For brevity, we use $P = n + 1$ to denote the number of control points.

We adopt a similar training process to [49], except that the networks are evaluated by different loss functions and the two end points of the curve are not trained in advance. We train the Bezier curve by optimizing all control points simultaneously. At each training step, we randomly sample a frame index t from all indices in a group, i.e., $t \sim \mathcal{U}(\mathcal{T})$, where

$$\mathcal{T} = \{0, 1, 2, \dots, T-1\}. \quad (33)$$

Then we obtain the sample points $\Theta^{(t)}$ from the control points, calculate the loss $\mathcal{L}_F^{(t)}(\Theta^{(t)})$, and update the control points with a gradient step.

The Bezier curve is controlled by very few control points but can connect much more densely distributed points in neural space. In other words, P can be much smaller than T . Therefore, the encoder quantizes and transmits the control points $\Theta_0, \Theta_1, \dots, \Theta_n$ instead of the sample points

$\Theta^{(0)}, \Theta^{(1)}, \dots, \Theta^{(T-1)}$, thus significantly reducing the bit rates. The overall loss function is formulated as

$$\mathcal{L}_F(\Theta_0, \dots, \Theta_n) = \mathbb{E}_{t \sim \mathcal{U}(\mathcal{T})} [\mathcal{L}_F^{(t)}(\Theta^{(t)})] + \frac{\lambda_F}{|\mathcal{X}^{(0)}| + \dots + |\mathcal{X}^{(T-1)}|} \sum_{i=0}^n \|\Theta_i\|_1. \quad (34)$$

The decoder receives the quantized control points $\widehat{\Theta}_0, \widehat{\Theta}_1, \dots, \widehat{\Theta}_n$, and then obtain the lossy sample points $\widehat{\Theta}^{(0)}, \widehat{\Theta}^{(1)}, \dots, \widehat{\Theta}^{(T-1)}$ in the same way as (32). They serve as the parameters of T networks that are utilized to reconstruct T point cloud frames in a group.

C. 4D Spatio-Temporal Representations

The aforementioned methods individually represent each point cloud frame using a neural network, as described in the previous section, and then focus on minimizing temporal redundancy of the network parameters within the neural space. An alternative approach is to directly address redundancy within the point cloud space itself by constructing a single neural field capable of simultaneously representing multiple point cloud frames.

Following the last subsection, we take consecutive T frames in the point cloud sequence as a group and encode each group individually. A group of T frames is equivalent to a 4D point cloud, with each point defined by its spatio-temporal coordinate (t, \mathbf{x}) , where $\mathbf{x} \in \mathcal{X}^{(t)}$ is a point in the t -th frame, and $t \in \mathcal{T}$ is the frame index. We define the geometry and attributes of a 4D point cloud as follows:

$$\overline{\mathcal{X}} = \{(t, \mathbf{x}) : \mathbf{x} \in \mathcal{X}^{(t)}, t \in \mathcal{T}\}, \quad (35)$$

$$\overline{C}(t, \mathbf{x}) = C^{(t)}(\mathbf{x}). \quad (36)$$

The entire voxelized 4D space contains $T \times 2^N \times 2^N \times 2^N$ 4D voxels. We partition the 4D space into $T \times 2^M \times 2^M \times 2^M$ cubes, each containing $1 \times 2^{N-M} \times 2^{N-M} \times 2^{N-M}$ voxels. Note that all voxels in the same cube share one temporal coordinate. The non-empty cubes and the voxels within these cubes in 4D space can be formulated as

$$\overline{\mathcal{W}} = \{(t, \mathbf{w}) : \mathbf{w} \in \mathcal{W}^{(t)}, t \in \mathcal{T}\}, \quad (37)$$

$$\overline{\mathcal{V}} = \{(t, \mathbf{x}) : \mathbf{x} \in \mathcal{V}^{(t)}, t \in \mathcal{T}\}. \quad (38)$$

Therefore, the INR of a single point cloud can be easily extended to representing several point cloud frames, resulting in much lower bit rates. We name this approach as 4D-NeRC³.

The geometry and attributes of the 4D point cloud are represented by two neural networks \overline{F} and \overline{G} , parameterized by $\overline{\Theta}$ and $\overline{\Phi}$ respectively. Both networks take spatio-temporal coordinates (t, \mathbf{x}) as input. When the temporal coordinate t is fixed, the two networks only process spatial coordinates and thus represent a single frame, regressing to 3D representations in the previous section. We follow the network structure depicted in Fig. 3. Note that positional encoding is applied separately to the spatial coordinate \mathbf{x} and temporal coordinate t . We select different values of L for the two encodings, denoted by L_x and L_t respectively, and concatenate the produced vectors together before feeding them into the first

fully-connected layer, as demonstrated in Fig. 3(c). In our experiment, we set $L_x = 12$ and $L_t = 4$.

When training \overline{F} , the ground-truth occupancy of a 4D voxel is the same whether in the corresponding 3D frame or in 4D space. However, the nearest neighbor of a 4D voxel is different in the two cases. When training \overline{G} , we let the expected color of a voxel match its nearest neighbor in the same frame, independent of other frames, since the overall attribute distortion of point clouds is evaluated for each frame individually. Further more, instead of utilizing a single threshold to reconstruct all frames, we allocate each frame a threshold $\tau^{(t)}$ for better reconstruction quality. By fixing the temporal coordinate t and following (10) and (14), we can reconstruct the t -th point cloud frame as

$$\widehat{\mathcal{X}}^{(t)} = \{\mathbf{x} : \overline{F}(t, \mathbf{x}; \widehat{\Theta}) > \tau^{(t)}, \mathbf{x} \in \mathcal{V}^{(t)}\}, \quad (39)$$

$$\widehat{C}^{(t)}(\widehat{\mathbf{x}}) = \overline{G}(t, \widehat{\mathbf{x}}; \widehat{\Phi}). \quad (40)$$

V. EXPERIMENTAL RESULTS

This section performs numerical experiments to verify the effectiveness of the proposed schemes.

A. Experimental Settings

We test our proposed methods on 8i Voxelized Full Bodies (8iVFB) [50], a dataset employed by the common testing conditions [43]. It contains 4 point cloud sequences, namely *longdress*, *loot*, *redandblack*, and *soldier*. Each sequence spans 10 seconds at a frame rate of 30 fps, thus comprising 300 frames. All these frames are voxelized with a 10-bit resolution. We test the first frame of each sequence to verify the performance of static PCC, and the first 32 frames of each sequence for dynamic PCC.

The 3D space for each frame is partitioned into $32 \times 32 \times 32$ cubes, i.e., $M = 5$. Both networks are trained using the Adam optimizer with weight decay 10^{-4} . We use a batch size of 4096 voxels. The first network F undergoes training for approximately 1200K steps, while the second network G is trained for about 800K steps. The learning rate is initialized to 10^{-3} and decays by a factor 0.1 every quarter of the entire training process. During training of F , we set $\alpha = \beta = 0.5$. We quantize the optimized network parameters of F and G with step sizes $\Delta_F = 1/1024$ and $\Delta_G = 1/4096$, respectively. Finally, we employ DeepCABAC [51] to losslessly compress the quantized parameters.

We adjust the parameter settings to achieve various bit rates. Note that we keep the regularization strengths λ_F and λ_G identical in each experiment. Hence, we use a single notation λ to refer to either of them.

- For NeRC³ (i-NeRC³), we adjust λ to achieve different bit rates. We set λ as 1, 5, 20, 50.
- For r-NeRC³, we set λ as 5, 20, 50.
- For c-NeRC³, we set $P = 3$ and $\lambda = 1$, and adjust T for various bit rates. The value of T is set as 8, 16, 32 for *soldier* and 4, 8, 16 for the other three sequences.
- For 4D-NeRC³, we use different (T, λ) pairs to attain the corresponding bit rates. The (T, λ) pair is set as (2, 1), (4, 1), (4, 10), (16, 10) for *longdress*,

TABLE II: Performance gains of the proposed method against G-PCC and V-PCC for static PCC.

Compression Scenario		G-PCC (octree+RAHT)		G-PCC (trisoup+RAHT)		V-PCC	
Point Cloud		BD-BR (%)	BD-PSNR (dB)	BD-BR (%)	BD-PSNR (dB)	BD-BR (%)	BD-PSNR (dB)
Geometry Alone	<i>longdress</i>	-70.28	7.61	94.14	-0.97	42.03	-2.01
	<i>loot</i>	-74.77	7.89	87.94	-1.08	47.33	-2.08
	<i>redandblack</i>	-64.14	6.07	153.59	-2.69	45.36	-2.44
	<i>soldier</i>	-72.37	7.51	71.68	-1.21	22.21	-1.03
	Average	-70.39	7.27	101.84	-1.49	39.23	-1.89
Point Cloud		BD-BR (%)	BD-PCQM (10^{-3})	BD-BR (%)	BD-PCQM (10^{-3})	BD-BR (%)	BD-PCQM (10^{-3})
Geometry & Attributes	<i>longdress</i>	-13.06	0.88	19.11	-0.59	75.07	-2.07
	<i>loot</i>	-37.01	3.71	143.20	-2.87	105.48	-2.96
	<i>redandblack</i>	-26.50	2.22	50.04	-1.25	65.00	-1.68
	<i>soldier</i>	-29.75	3.14	84.37	-2.10	60.93	-2.08
	Average	-26.58	2.49	74.18	-1.70	76.62	-2.20

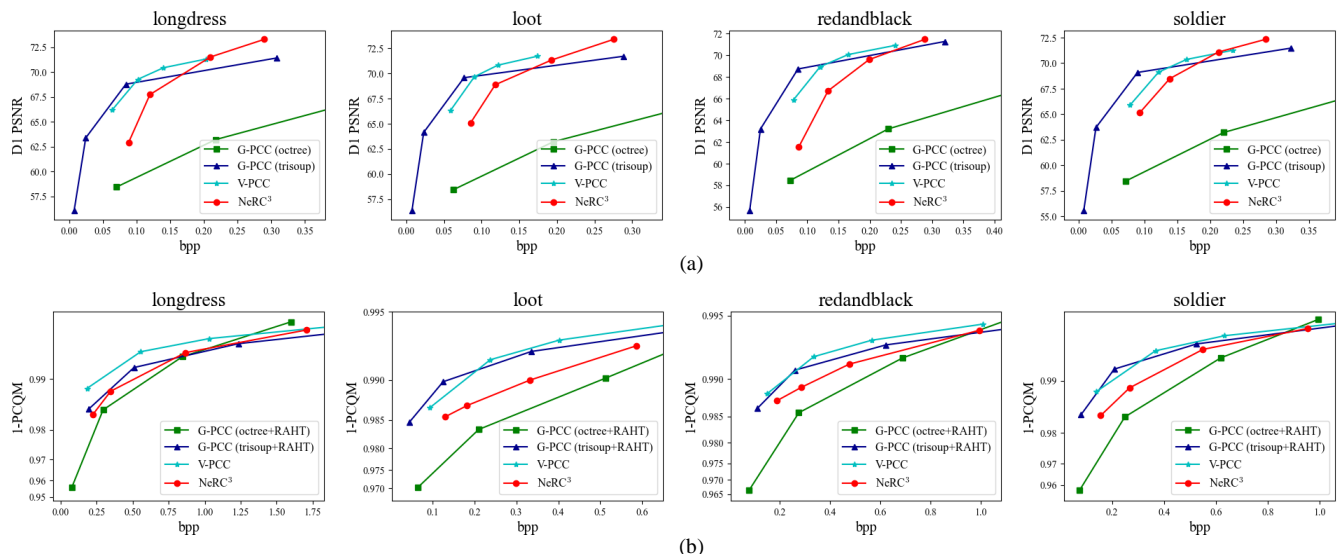


Fig. 5: Rate-distortion curves of the proposed method and baselines for static PCC. (a) Geometry compression performance, distortion measured by D1 PSNR. (b) Joint compression performance, distortion measured by PCQM.

(2, 1), (4, 1), (8, 1), (16, 10) for *loot* and *redandblack*, and (2, 1), (4, 1), (8, 1), (32, 1) for *soldier*.

We compare our methods with the latest version of MPEG PCC test models, including TMC13-v23.0-rc2 for G-PCC [52] and TMC2-v24.0 for V-PCC [53]. Because G-PCC encodes the geometry and attributes separately, we employ G-PCC (octree) and G-PCC (trisoup) for geometry compression and G-PCC (RAHT) for attribute compression. For V-PCC, we set the mode to *all-intra* for intra-frame compression and *random-access* for inter-frame compression. We set the parameters of these baselines following the common testing conditions [43].

As mentioned before, we measure the geometry distortion by D1 PSNR and use PCQM [44] to assess the overall distortion. The compressed bit rate is defined as bits per point (bpp). For performance comparison, we employ Bjontegaard delta metrics [54] to quantify the rate-distortion performance gains of different methods.

B. Performance

1) *Static PCC*: We first compare the performance of NeRC³ against the baselines when compressing static point clouds. We set the mode for V-PCC as *all-intra*. The performance gains are presented in Table. II. For geometry compression alone, NeRC³ surpasses G-PCC (octree) by an averaged 70.39% BD-BR gain. However, it suffers significant performance losses compared with G-PCC (trisoup) and V-PCC, i.e., 101.84% and 39.23% BD-BR losses, respectively. This is caused by the inferior performance at low bit rates, as shown in Fig. 5(a). In terms of overall performance of compressing both geometry and attributes, NeRC³ outperforms G-PCC (octree+RAHT) with an averaged 26.58% BD-BR gain but suffers 74.18% and 76.62% BD-BR losses compared with G-PCC (trisoup+RAHT) and V-PCC.

2) *Dynamic PCC*: Since we proposed three approaches, namely r-NeRC³, c-NeRC³, and 4D-NeRC³, to exploit the temporal correlations, we first demonstrate the performance gains of these extended methods against the intra-frame compression method, i-NeRC³. The results are presented in Table

TABLE III: Performance gains of three extended methods against the intra-frame compression method.

Compression Scenario	r-NeRC ³		c-NeRC ³		4D-NeRC ³		
	Point Cloud	BD-BR (%)	BD-PSNR (dB)	BD-BR (%)	BD-PSNR (dB)	BD-BR (%)	BD-PSNR (dB)
Geometry Alone	<i>longdress</i>	25.10	-1.65	-64.97	1.54	-51.13	3.62
	<i>loot</i>	27.54	-1.49	-13.87	0.39	-54.29	3.55
	<i>redandblack</i>	21.41	-1.43	-17.95	1.27	-41.09	3.13
	<i>soldier</i>	28.39	-1.63	-51.06	2.51	-78.48	4.54
	Average	25.61	-1.55	-36.96	1.43	-56.25	3.71
Geometry & Attributes	Point Cloud	BD-BR (%)	BD-PCQM (10 ⁻³)	BD-BR (%)	BD-PCQM (10 ⁻³)	BD-BR (%)	BD-PCQM (10 ⁻³)
	<i>longdress</i>	11.92	-0.59	-36.02	1.30	-41.34	2.13
	<i>loot</i>	1.86	-0.10	-74.57	1.93	-62.08	3.42
	<i>redandblack</i>	5.81	-0.22	-22.76	1.26	-51.13	2.31
	Average	7.29	-0.36	-51.64	2.70	-63.45	3.39

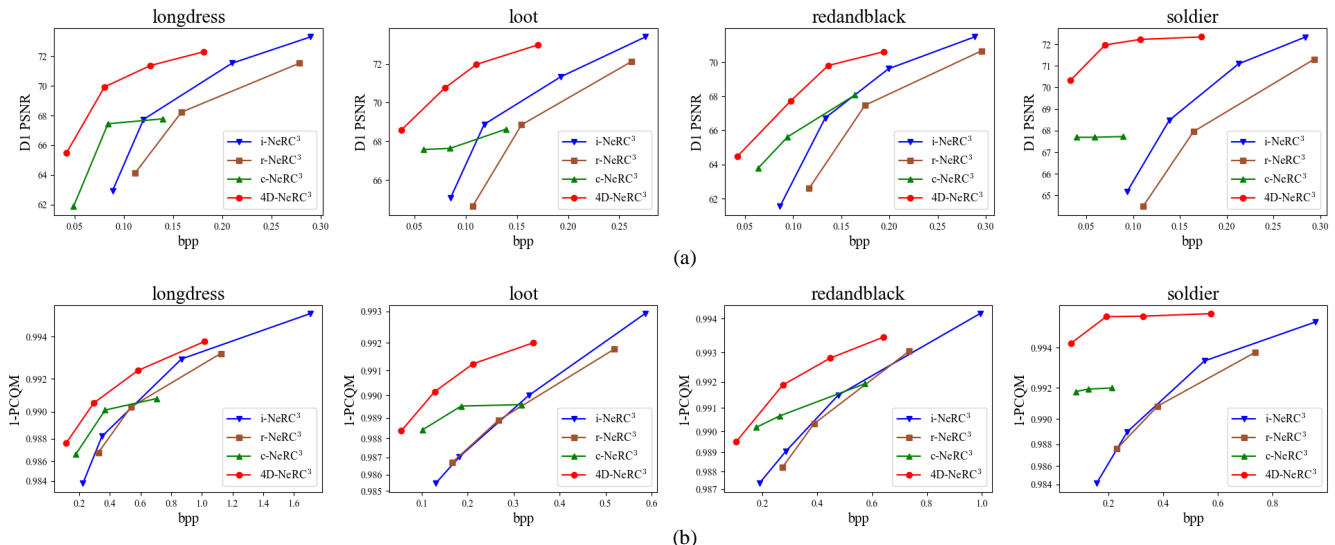


Fig. 6: Rate-distortion curves of three extended methods and the intra-frame compression method. (a) Geometry compression performance, distortion measured by D1 PSNR. (b) Joint compression performance, distortion measured by PCQM.

III. For geometry compression alone, residual compression achieves inferior performance with an averaged 25.61% BD-BR loss, due to significant difference of voxel occupancies between successive point cloud frames. In contrast, c-NeRC³ and 4D-NeRC³ successfully reduce the temporal redundancy and outperform intra-frame compression by averaged 36.96% and 56.25% BD-BR gains respectively. Similarly, for joint geometry and attribute compression, r-NeRC³ suffers an averaged 7.29% BD-BR loss, while c-NeRC³ and 4D-NeRC³ attains 51.64% and 63.45% BD-BR gains over intra-frame compression. Rate-distortion curves in Fig. 6 further demonstrate that 4D-NeRC³ achieves the leading performance among the four methods. c-NeRC³, despite performance gains over i-NeRC³, only applies to low bit rates due to the large value of T , and still suffers performance losses compared with 4D-NeRC³.

Now we compare 4D-NeRC³, which achieves the leading performance among three extended methods, with the baselines. The performance gains are presented in Table. IV. For geometry compression, 4D-NeRC³ outperforms all the base-

lines. It gains 89.07% BD-BR over G-PCC (octree), 29.24% over G-PCC (trisoup), 39.95% over V-PCC (intra), and 23.34% over V-PCC (inter). For overall performance of compressing both geometry and attributes, 4D-NeRC³ surpasses G-PCC (octree+RAHT), G-PCC (trisoup+RAHT) and V-PCC (intra), with averaged 71.05%, 41.30% and 28.61% BD-BR gains, respectively. Although 4D-NeRC³ has an averaged 21.46% BD-BR loss compared with V-PCC (inter), it reports significant 93.83% BD-BR gains on *soldier*. The rate-distortion curves are plotted in Fig. 7, where we can see that 4D-NeRC³ achieves high performance on *soldier* even at very low bit rates.

In fact, there is an interesting finding that c-NeRC³ and 4D-NeRC³ maintain nearly constant distortion over a wide range of bit rates when evaluated on *soldier*. This is because the sequence is more static in the first 32 frames than the other three sequences, containing more temporal redundancy. Our methods can efficiently capture the similarities across these frames, resulting in much lower bit rates without rapid degradation in reconstruction quality.

TABLE IV: Performance gains of the proposed method against G-PCC and V-PCC for dynamic PCC.

Compression Scenario		G-PCC (octree+RAHT)		G-PCC (trisoup+RAHT)		V-PCC (intra)		V-PCC (inter)	
Point Cloud		BD-BR (%)	BD-PSNR (dB)	BD-BR (%)	BD-PSNR (dB)	BD-BR (%)	BD-PSNR (dB)	BD-BR (%)	BD-PSNR (dB)
Geometry Alone	<i>longdress</i>	-88.33	10.74	-26.87	1.04	-33.46	1.59	-25.73	1.18
	<i>loot</i>	-91.24	11.30	-40.58	1.35	-38.76	1.77	-5.93	0.37
	<i>redandblack</i>	-81.65	8.56	34.03	-1.14	-5.68	0.25	5.79	-0.20
	<i>soldier</i>	-95.04	12.12	-83.52	3.52	-81.89	3.59	-67.49	2.21
	Average	-89.07	10.68	-29.24	1.19	-39.95	1.80	-23.34	0.89
Point Cloud		BD-BR (%)	BD-PCQM (10^{-3})	BD-BR (%)	BD-PCQM (10^{-3})	BD-BR (%)	BD-PCQM (10^{-3})	BD-BR (%)	BD-PCQM (10^{-3})
Geometry & Attributes	<i>longdress</i>	-49.02	6.66	-29.55	1.45	19.72	-0.43	66.58	-1.49
	<i>loot</i>	-74.40	10.78	-9.20	0.45	-18.83	0.47	103.05	-2.44
	<i>redandblack</i>	-62.28	7.85	-28.05	1.20	-17.10	0.50	10.04	0.02
	<i>soldier</i>	-98.49	16.31	-98.40	4.39	-98.24	3.21	-93.83	1.01
	Average	-71.05	10.40	-41.30	1.87	-28.61	0.94	21.46	-0.73

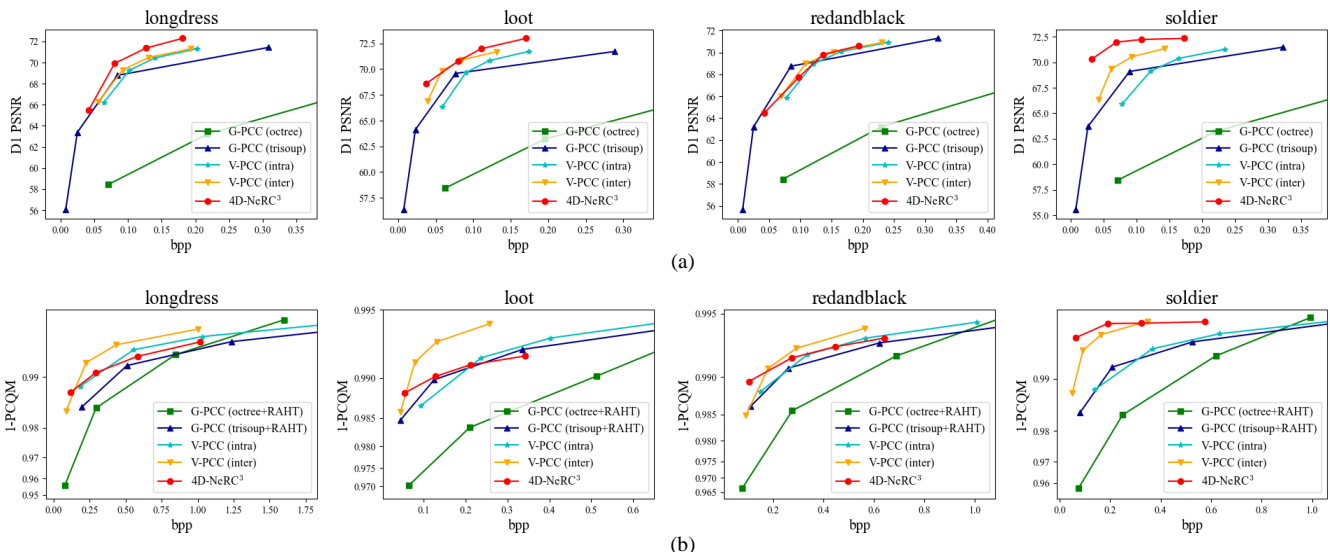


Fig. 7: Rate-distortion curves of the proposed method and baselines for dynamic PCC. (a) Geometry compression performance, distortion measured by D1 PSNR. (b) Joint compression performance, distortion measured by PCQM.

C. Ablation Studies

In this subsection, we investigate the effectiveness of different aspects in our proposed framework NeRC³. We conduct our studies on the first frame of *longdress*.

1) *Network Structure*: To demonstrate the benefits of the adopted positional encoding and layer normalization in the network structure, we remove the two components separately, obtaining two variations of the network structure. With other experimental settings unchanged, we compress both geometry and attributes of the first frame in *longdress* using the proposed network structure and its variations. Rate-distortion curves in Fig. 8(a) evidence that both positional encoding and layer normalization enhance the networks' capacity to achieve higher performance.

Additionally, we use the sine function [46] as the core activation for network *G*. We replace it with the ReLU activation to assess its effect on the rate-distortion performance. The results are depicted in Fig. 8(b). We can see that the sine activation achieves superior performance over the ReLU activation. In fact, the sine activation plays a similar role to

positional encoding. By expanding the outputs of hidden layers to several periods and passing them through a periodic function, it introduces high-frequency information in the middle of the network, as done by positional encoding at the input.

2) *Sampling Strategy*: As mentioned before, we introduce a hyperparameter β controlling the ratio of occupied voxels in training samples. To explore the effect of different values of β , we perform geometry compression with $\beta = 0.5, 0.1$ and ζ , where $\beta = \zeta$ implies uniform voxel sampling across the volumetric space. Meanwhile, we adjust the settings for λ to attain a similar range of bit rate variation for different β s. A comparison of the performance is shown in Fig. 8(c). Notably, sampling with a larger β exhibits superior performance over uniform sampling, particularly at higher bit rates. It's worth noting that when $\beta = 0.5$, the balancing between two classes of voxels is of no practical help since they have equal weights. Hence, our experiments demonstrate that adjusting the sampling ratios of different classes may be more effective than weighting their loss functions.

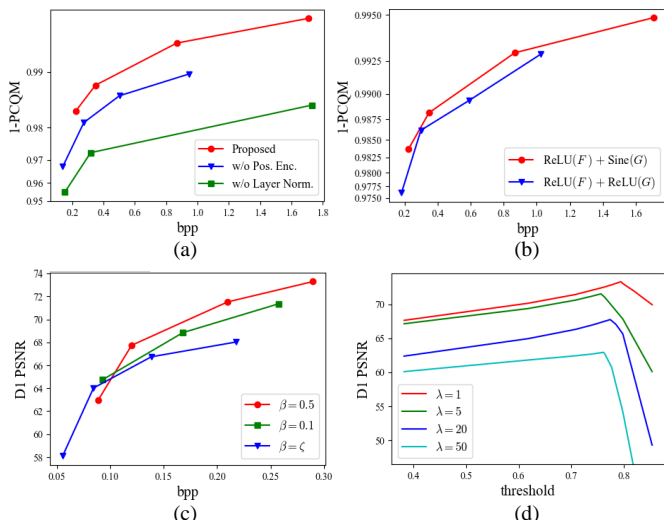


Fig. 8: Ablation studies on the first frame of *longdress*. (a)-(b) Rate-distortion performance for joint geometry and attribute compression using different variations of the network structure. (c) Rate-distortion performance for geometry compression when $\beta = 0.5, 0.1$ and ζ . (d) Geometry distortion functions with regard to the threshold.

3) *Threshold Finetuning*: When reconstructing the occupied voxels, we introduce a threshold τ to determine whether a voxel is occupied or not. In Section III-E, we claim that the geometry distortion (i.e., DI PSNR) is a unimodal function of τ . To assess the impact of this threshold and validate our proposition, we train a network F with each λ and then evaluate the reconstruction quality over a range of thresholds. We plot the geometry distortion functions for different λ s in Fig. 8(d). The result confirms that the geometry distortion is unimodal, and the optimal threshold varies across different networks.

VI. CONCLUSION

In this paper, we proposed NeRC³, a novel framework for PCC based on INRs. Our approach initially targeted the compression of a single point cloud by employing two neural networks to implicitly represent its geometry and attributes, respectively. This representation was followed by parameter quantization and encoding, with the quantized parameters and auxiliary information enabling the reconstruction of a lossy version of the original point cloud. Furthermore, we extended our method to dynamic PCC, proposing several strategies to exploit temporal redundancy in point cloud sequences, including a 4D spatial-temporal representation approach (4D-NeRC³). Extensive experimental results demonstrated the effectiveness of our frameworks.

This work paves a new path for INR-based PCC, supporting the compression of both geometry and attributes for static and dynamic point clouds. Future research can focus on enhancing the rate-distortion performance by exploring more efficient network architectures and training strategies. Additionally, the time and space complexity of INR-based methods can be further reduced by leveraging advanced techniques from other fields, such as fast neural rendering.

APPENDIX A PROOF OF PROPOSITION 1

When reconstructing the geometry of a point cloud, we first obtain the OPs $\hat{p}(\mathbf{x})$ of all voxels in \mathcal{V} by feeding each \mathbf{x} into F . It's worth noting that none of these OPs is strictly equal to 0 or 1 because the output value of F is the sigmoid function. We sort these OPs in ascending order and remove the duplicate values, yielding a sequence $0 < p_1 < p_2 < \dots < p_K < 1$. These OPs segment the interval $[0, 1]$ into $K + 1$ subintervals, namely $[0, p_1), [p_1, p_2), \dots, [p_{K-1}, p_K), [p_K, 1]$.

Let $\tau_{\max} = p_K$. If τ lies in the last subinterval, i.e., $\tau \geq \tau_{\max}$, there is no voxel that has an OP greater than the threshold. In this case, the reconstructed point cloud contains no points and $D(\tau)$ is not defined. Otherwise, τ must lie in one of the remaining K subintervals. We consider any one of these subintervals, denoted by $[p_{i-1}, p_i)$, $i = 1, 2, \dots, K$, where we define $p_0 = 0$ for generality. If τ lies in $[p_{i-1}, p_i)$, then only the voxels with OPs p_i, p_{i+1}, \dots, p_K will be reconstructed as occupied. Therefore, $D(\tau)$ remains constant within this subinterval. Furthermore, $D(\tau)$ is also right-continuous because $\tau + \delta$ still lies in the same subinterval for sufficiently small $\delta > 0$, such as $\delta = (p_i - \tau)/2$. But $D(\tau)$ may not be left-continuous at the boundary $\tau = p_{i-1}$, $i = 2, 3, \dots, K$, because no matter how small δ is, $p_{i-1} - \delta$ will move into another subinterval $[p_{i-2}, p_{i-1})$, where the voxel(s) with OP p_{i-1} will additionally be reconstructed, which may change the value of $D(\tau)$.

APPENDIX B PROOF OF PROPOSITION 2

Following the proof of Proposition 1, we sort all possible values of $\hat{p}(\mathbf{x})$ in ascending order as $p_1 < p_2 < \dots < p_K$, where $p_K = \tau_{\max}$. Also, we define $p_0 = 0$. Then the interval $[0, \tau_{\max})$ is segmented into K subintervals $[p_0, p_1), [p_1, p_2), \dots, [p_{K-1}, p_K)$. Let $\hat{\mathcal{X}}_i$ be the reconstructed point cloud when τ lies in $[p_{i-1}, p_i)$, $i = 1, 2, \dots, K$. Apparently, $\hat{\mathcal{X}}_i$ contains the voxels with OPs p_i, p_{i+1}, \dots, p_K . In the following, we consider $e(\hat{\mathcal{X}}_i, \mathcal{X})$ and $e(\mathcal{X}, \hat{\mathcal{X}}_i)$ as two sequences indexed by $i = 1, 2, \dots, K$, and complete our proof in five steps.

Step 1: $e(\hat{\mathcal{X}}_i, \mathcal{X})$ is non-increasing.

For $i = 1, 2, \dots, K - 1$, $\hat{\mathcal{X}}_i$ can be divided into $\hat{\mathcal{X}}_{i+1}$ and $\delta\hat{\mathcal{X}}_i = \hat{\mathcal{X}}_i - \hat{\mathcal{X}}_{i+1}$, where the former contains voxels with OPs p_{i+1}, \dots, p_K and the latter contains the voxel(s) with OP p_i . By assumption 2), we have

$$d(\mathbf{x}_0, \mathcal{X}) \geq \mathbb{E}_{\mathbf{x} \sim \mathcal{U}(\hat{\mathcal{X}}_{i+1})}[d(\mathbf{x}, \mathcal{X})], \quad \forall \mathbf{x}_0 \in \delta\hat{\mathcal{X}}_i.$$

Then we average $d(\mathbf{x}_0, \mathcal{X})$ for \mathbf{x}_0 over $\delta\hat{\mathcal{X}}_i$ and get

$$\mathbb{E}_{\mathbf{x} \sim \mathcal{U}(\delta\hat{\mathcal{X}}_i)}[d(\mathbf{x}, \mathcal{X})] \geq \mathbb{E}_{\mathbf{x} \sim \mathcal{U}(\hat{\mathcal{X}}_{i+1})}[d(\mathbf{x}, \mathcal{X})].$$

Meanwhile, it holds that

$$\begin{aligned} & \mathbb{E}_{\mathbf{x} \sim \mathcal{U}(\hat{\mathcal{X}}_i)}[d(\mathbf{x}, \mathcal{X})] \\ &= \frac{|\delta\hat{\mathcal{X}}_i|}{|\hat{\mathcal{X}}_i|} \mathbb{E}_{\mathbf{x} \sim \mathcal{U}(\delta\hat{\mathcal{X}}_i)}[d(\mathbf{x}, \mathcal{X})] + \frac{|\hat{\mathcal{X}}_{i+1}|}{|\hat{\mathcal{X}}_i|} \mathbb{E}_{\mathbf{x} \sim \mathcal{U}(\hat{\mathcal{X}}_{i+1})}[d(\mathbf{x}, \mathcal{X})] \\ &\geq \mathbb{E}_{\mathbf{x} \sim \mathcal{U}(\hat{\mathcal{X}}_{i+1})}[d(\mathbf{x}, \mathcal{X})], \end{aligned}$$

or equivalently,

$$e(\widehat{\mathcal{X}}_i, \mathcal{X}) \geq e(\widehat{\mathcal{X}}_{i+1}, \mathcal{X}), \quad (41)$$

where $e(\cdot, \cdot)$ is the point-to-point error, as defined in (2).

Step 2: $e(\mathcal{X}, \widehat{\mathcal{X}}_i)$ is non-decreasing.

Similar to the previous step, we divide $\widehat{\mathcal{X}}_i$ into $\widehat{\mathcal{X}}_{i+1}$ and $\delta\widehat{\mathcal{X}}_i$, $i = 1, 2, \dots, K-1$. By the definition of $d(\cdot, \cdot)$, we have

$$\begin{aligned} d(\mathbf{x}_0, \widehat{\mathcal{X}}_i) &= \min\{d(\mathbf{x}_0, \delta\widehat{\mathcal{X}}_i), d(\mathbf{x}_0, \widehat{\mathcal{X}}_{i+1})\} \\ &\leq d(\mathbf{x}_0, \widehat{\mathcal{X}}_{i+1}), \quad \forall \mathbf{x}_0. \end{aligned}$$

By averaging $d(\mathbf{x}_0, \widehat{\mathcal{X}}_i)$ and $d(\mathbf{x}_0, \widehat{\mathcal{X}}_{i+1})$ separately for \mathbf{x}_0 over \mathcal{X} , we can get

$$e(\mathcal{X}, \widehat{\mathcal{X}}_i) \leq e(\mathcal{X}, \widehat{\mathcal{X}}_{i+1}). \quad (42)$$

Step 3: The minimum value of $e(\widehat{\mathcal{X}}_i, \mathcal{X})$ is 0.

Because $e(\widehat{\mathcal{X}}_i, \mathcal{X})$ is non-increasing, the minimum value is achieved when $i = K$. Note that $\widehat{\mathcal{X}}_K$ equals $\widehat{\mathcal{X}}_{\max}$ that is defined in assumption 1).

Suppose that there exists a voxel \mathbf{x}_1 in $\widehat{\mathcal{X}}_K$ but not in \mathcal{X} . Then there must exist another voxel \mathbf{x}_0 in \mathcal{X} but not in $\widehat{\mathcal{X}}_K$ because by assumption 1), \mathcal{X} contains at least the same number of voxels as $\widehat{\mathcal{X}}_K$. We write the relationships below:

$$\mathbf{x}_1 \in \widehat{\mathcal{X}}_K, \quad \mathbf{x}_1 \notin \mathcal{X}, \quad \mathbf{x}_0 \in \mathcal{X}, \quad \mathbf{x}_0 \notin \widehat{\mathcal{X}}_K.$$

$\mathbf{x}_1 \in \widehat{\mathcal{X}}_K$ implies that \mathbf{x}_1 has the highest OP, while $\mathbf{x}_0 \notin \widehat{\mathcal{X}}_K$ implies that its OP is lower than \mathbf{x}_1 . Hence, we have $\mathbf{x}_1 \in \mathcal{X}_h(\mathbf{x}_0)$. Meanwhile, $\mathbf{x}_0 \in \mathcal{X}$ implies $d(\mathbf{x}_0, \mathcal{X}) = 0$, and $\mathbf{x}_1 \notin \mathcal{X}$ implies $d(\mathbf{x}_1, \mathcal{X}) > 0$, where the latter derives $\mathbb{E}_{\mathbf{x} \sim \mathcal{U}(\widehat{\mathcal{X}}_h(\mathbf{x}_0))}[d(\mathbf{x}, \mathcal{X})] > 0$. Therefore, we have

$$d(\mathbf{x}_0, \mathcal{X}) < \mathbb{E}_{\mathbf{x} \sim \mathcal{U}(\widehat{\mathcal{X}}_h(\mathbf{x}_0))}[d(\mathbf{x}, \mathcal{X})].$$

However, by assumption 2) we have

$$d(\mathbf{x}_0, \mathcal{X}) \geq \mathbb{E}_{\mathbf{x} \sim \mathcal{U}(\widehat{\mathcal{X}}_h(\mathbf{x}_0))}[d(\mathbf{x}, \mathcal{X})].$$

This leads to a contradiction. Therefore, such \mathbf{x}_1 does not exist, or in other words, $\widehat{\mathcal{X}}_K$ must be a subset of \mathcal{X} . Then $d(\mathbf{x}_0, \mathcal{X}) = 0, \forall \mathbf{x}_0 \in \widehat{\mathcal{X}}_K$, and thus

$$e(\widehat{\mathcal{X}}_K, \mathcal{X}) = 0. \quad (43)$$

Step 4: The minimum value of $e(\mathcal{X}, \widehat{\mathcal{X}}_i)$ is 0.

$e(\mathcal{X}, \widehat{\mathcal{X}}_i)$ achieves its minimum when $i = 1$. By definition, $\widehat{\mathcal{X}}_1 = \mathcal{V}$. Apparently \mathcal{X} is a subset of $\widehat{\mathcal{X}}_1$, and similarly we have

$$e(\mathcal{X}, \widehat{\mathcal{X}}_1) = 0. \quad (44)$$

Step 5: $D(\tau)$ is unimodal.

By combining (41)-(44), we can get

$$e(\widehat{\mathcal{X}}_K, \mathcal{X}) \leq e(\mathcal{X}, \widehat{\mathcal{X}}_K), \quad e(\widehat{\mathcal{X}}_1, \mathcal{X}) \geq e(\mathcal{X}, \widehat{\mathcal{X}}_1).$$

Therefore, there must exist some $I \in \{1, 2, \dots, K-1\}$ such that:

- For $i = 1, \dots, I$, $e(\widehat{\mathcal{X}}_i, \mathcal{X}) \geq e(\mathcal{X}, \widehat{\mathcal{X}}_i)$. Thus $\max\{e(\widehat{\mathcal{X}}_i, \mathcal{X}), e(\mathcal{X}, \widehat{\mathcal{X}}_i)\} = e(\widehat{\mathcal{X}}_i, \mathcal{X})$ is non-increasing.
- For $i = I+1, \dots, K$, $e(\widehat{\mathcal{X}}_i, \mathcal{X}) \leq e(\mathcal{X}, \widehat{\mathcal{X}}_i)$. Thus $\max\{e(\widehat{\mathcal{X}}_i, \mathcal{X}), e(\mathcal{X}, \widehat{\mathcal{X}}_i)\} = e(\mathcal{X}, \widehat{\mathcal{X}}_i)$ is non-decreasing.

By the definition of D1 PSNR in (3), we have

$$D(\tau) = 10 \log_{10} \frac{3 \times (2^N - 1)^2}{\max\{e(\widehat{\mathcal{X}}_i, \mathcal{X}), e(\mathcal{X}, \widehat{\mathcal{X}}_i)\}}, \quad \tau \in [p_{i-1}, p_i].$$

Let $\tau^* = p_I$. Then $D(\tau)$ is non-decreasing on $[0, \tau^*)$ and non-increasing on $(\tau^*, \tau_{\max}]$.

REFERENCES

- [1] D. Graziosi, O. Nakagami, S. Kuma, A. Zaghetto, T. Suzuki, and A. Tabatabai, "An overview of ongoing point cloud compression standardization activities: Video-based (V-PCC) and geometry-based (G-PCC)," *APSIPA Trans. Signal Inf. Proc.*, vol. 9, no. 1, 2020.
- [2] J. Wang, H. Zhu, H. Liu, and Z. Ma, "Lossy point cloud geometry compression via end-to-end learning," *IEEE Trans. Circuits Syst. Video Tech.*, vol. 31, no. 12, pp. 4909–4923, 2021.
- [3] Y. Shao, C. Bian, L. Yang, Q. Yang, Z. Zhang, and D. Gunduz, "Point cloud in the air," *arXiv:2401.00658*, 2024.
- [4] H. Ruan, Y. Shao, Q. Yang, L. Zhao, and D. Niyato, "Point cloud compression with implicit neural representations: A unified framework," in *IEEE/CIC ICC*, 2024.
- [5] J. Wang, D. Ding, Z. Li, and Z. Ma, "Multiscale point cloud geometry compression," in *Proc. Data Compression Conf. (DCC)*, 2021.
- [6] G. Liu, J. Wang, D. Ding, and Z. Ma, "PCGFormer: Lossy point cloud geometry compression via local self-attention," in *Proc. IEEE Int. Conf. Vis. Commun. Image Process. (VCIP)*, 2022.
- [7] J. Wang, D. Ding, Z. Li, X. Feng, C. Cao, and Z. Ma, "Sparse tensor-based multiscale representation for point cloud geometry compression," *IEEE Trans. Pattern Anal. Mach. Intell.*, vol. 45, no. 7, pp. 9055–9071, 2023.
- [8] J. Wang and Z. Ma, "Sparse tensor-based point cloud attribute compression," in *MIPR*, 2022, pp. 59–64.
- [9] J. Zhang, J. Wang, D. Ding, and Z. Ma, "Scalable point cloud attribute compression," *IEEE Trans. Multimedia*, 2023.
- [10] T. Huang and Y. Liu, "3D point cloud geometry compression on deep learning," in *Proc. ACM Int. Conf. Multimed. (MM)*, 2019, pp. 890–898.
- [11] X. Sheng, L. Li, D. Liu, Z. Xiong, Z. Li, and F. Wu, "Deep-PCAC: An end-to-end deep lossy compression framework for point cloud attributes," *IEEE Trans. Multimedia*, vol. 24, pp. 2617–2632, 2021.
- [12] C. Bian, Y. Shao, and D. Gündüz, "Wireless point cloud transmission," in *IEEE SPAWC*, 2024, pp. 851–855.
- [13] E. Alexiou, K. Tung, and T. Ebrahimi, "Towards neural network approaches for point cloud compression," in *Proc. SPIE Int. Soc. Opt. Eng.*, 2020, pp. 18–37.
- [14] L. Mescheder, M. Oechsle, M. Niemeyer, S. Nowozin, and A. Geiger, "Occupancy networks: Learning 3D reconstruction in function space," in *Proc. IEEE Comput. Soc. Conf. Comput. Vision Pattern Recognit. (CVPR)*, 2019, pp. 4460–4470.
- [15] Z. Chen and H. Zhang, "Learning implicit fields for generative shape modeling," in *Proc. IEEE Comput. Soc. Conf. Comput. Vision Pattern Recognit. (CVPR)*, 2019, pp. 5939–5948.
- [16] B. Mildenhall, P. P. Srinivasan, M. Tancik, J. T. Barron, R. Ramamoorthi, and R. Ng, "NeRF: Representing scenes as neural radiance fields for view synthesis," *Commun. ACM*, vol. 65, no. 1, pp. 99–106, 2021.
- [17] E. Dupont, A. Goliński, M. Alizadeh, Y. W. Teh, and A. Doucet, "COIN: Compression with implicit neural representations," *arXiv preprint arXiv:2103.03123*, 2021.
- [18] E. Dupont, H. Loya, M. Alizadeh, A. Goliński, Y. W. Teh, and A. Doucet, "COIN++: Neural compression across modalities," *arXiv preprint arXiv:2201.12904*, 2022.
- [19] Y. Strümpfer, J. Postels, R. Yang, L. V. Gool, and F. Tombari, "Implicit neural representations for image compression," in *Proc. Eur. Conf. Comput. Vis. (ECCV)*, 2022, pp. 74–91.
- [20] H. Chen, B. He, H. Wang, Y. Ren, S. N. Lim, and A. Shrivastava, "NeRV: Neural representations for videos," in *Proc. Adv. Neural Inf. Proces. Syst. (NeurIPS)*, 2021, pp. 21 557–21 568.
- [21] Y. Hu and Y. Wang, "Learning neural volumetric field for point cloud geometry compression," in *Proc. Pict. Coding Symp. (PCS)*, 2022, pp. 127–131.
- [22] B. Isik, P. A. Chou, S. J. Hwang, N. Johnston, and G. Toderici, "LVAC: Learned volumetric attribute compression for point clouds using coordinate based networks," *Front. Signal Process.*, vol. 2, p. 1008812, 2022.

- [23] F. Pistilli, D. Valsesia, G. Fracastoro, and E. Magli, "Signal compression via neural implicit representations," in *Proc. IEEE Int. Conf. Acoust. Speech Signal Process. (ICASSP)*, 2022, pp. 3733–3737.
- [24] G. J. Sullivan, J.-R. Ohm, W.-J. Han, and T. Wiegand, "Overview of the high efficiency video coding (HEVC) standard," *IEEE Trans. Circuits Syst. Video Technol.*, vol. 22, no. 12, pp. 1649–1668, 2012.
- [25] R. L. De Queiroz and P. A. Chou, "Compression of 3D point clouds using a region-adaptive hierarchical transform," *IEEE Trans. Image Process.*, vol. 25, no. 8, pp. 3947–3956, 2016.
- [26] J. Ballé, V. Laparra, and E. P. Simoncelli, "End-to-end optimized image compression," *arXiv:1611.01704*, 2016.
- [27] J. Ballé, D. Minnen, S. Singh, S. J. Hwang, and N. Johnston, "Variational image compression with a scale hyperprior," *arXiv:1802.01436*, 2018.
- [28] D. Minnen, J. Ballé, and G. D. Toderici, "Joint autoregressive and hierarchical priors for learned image compression," in *Proc. Adv. Neural Inf. Process. Syst. (NeurIPS)*, 2018, pp. 10771–10780.
- [29] Y. Shao, Q. Cao, and D. Gündüz, "A theory of semantic communication," *IEEE Transactions on Mobile Computing*, 2024.
- [30] Y. Hu, W. Yang, and J. Liu, "Coarse-to-fine hyper-prior modeling for learned image compression," in *Proc. AAAI Conf. Artif. Intell.*, 2020, pp. 11 013–11 020.
- [31] T. Fan, L. Gao, Y. Xu, Z. Li, and D. Wang, "D-DPCC: Deep dynamic point cloud compression via 3D motion prediction," *arXiv preprint arXiv:2205.01135*, 2022.
- [32] Z. Jiang, G. Wang, G. K. Tam, C. Song, F. W. Li, and B. Yang, "An end-to-end dynamic point cloud geometry compression in latent space," *Displays*, vol. 80, p. 102528, 2023.
- [33] A. Akhtar, Z. Li, and G. Van der Auwera, "Inter-frame compression for dynamic point cloud geometry coding," *IEEE Trans. Image Process.*, vol. 33, pp. 584–594, 2024.
- [34] Z. Pan, M. Xiao, X. Han, D. Yu, G. Zhang, and Y. Liu, "patchDPCC: A patchwise deep compression framework for dynamic point clouds," in *Proc. AAAI Conf. Artif. Intell.*, 2024, pp. 4406–4414.
- [35] J. J. Park, P. Florence, J. Straub, R. Newcombe, and S. Lovegrove, "DeepSDF: Learning continuous signed distance functions for shape representation," in *Proc. IEEE Comput. Soc. Conf. Comput. Vision Pattern Recognit. (CVPR)*, 2019, pp. 165–174.
- [36] C. Jiang, A. Sud, A. Makadia, J. Huang, M. Nießner, T. Funkhouser *et al.*, "Local implicit grid representations for 3D scenes," in *Proc. IEEE Comput. Soc. Conf. Comput. Vision Pattern Recognit. (CVPR)*, 2020, pp. 6001–6010.
- [37] H. Wu, M. Zhang, Y. Shao, K. Mikolajczyk, and D. Gündüz, "MIMO channel as a neural function: Implicit neural representations for extreme csi compression in massive MIMO systems," *arXiv:2403.13615*, 2024.
- [38] S. R. Maiya, S. Girish, M. Ehrlich, H. Wang, K. S. Lee, P. Poirson, P. Wu, C. Wang, and A. Shrivastava, "NIRVANA: Neural implicit representations of videos with adaptive networks and autoregressive patch-wise modeling," in *Proc. IEEE Comput. Soc. Conf. Comput. Vision Pattern Recognit. (CVPR)*, 2023, pp. 14 378–14 387.
- [39] R. Xue, J. Li, T. Chen, D. Ding, X. Cao, and Z. Ma, "NeRI: Implicit neural representation of LiDAR point cloud using range image sequence," in *Proc. IEEE Int. Conf. Acoust. Speech Signal Process. (ICASSP)*, 2024, pp. 8020–8024.
- [40] T. Bird, J. Ballé, S. Singh, and P. A. Chou, "3D scene compression through entropy penalized neural representation functions," in *Proc. Pict. Coding Symp. (PCS)*, 2021.
- [41] T. Takikawa, A. Evans, J. Tremblay, T. Müller, M. McGuire, A. Jacobson, and S. Fidler, "Variable bitrate neural fields," in *Proc. Spec. Int. Group Comp. Graph. Interact. Tech. Conf. (SIGGRAPH)*, 2022.
- [42] Y. Shi, R. Zhao, S. Gasparini, G. Morin, and W. T. Ooi, "Volumetric video compression through neural-based representation," in *Proc. Int. Workshop Immersive Mixed Virtual Environ. Syst. (MMVE)*, 2024, pp. 85–91.
- [43] S. Schwarz, G. Martin-Cocher, D. Flynn, and M. Budagavi, "Common test conditions for point cloud compression," *Document ISO/IEC JTC1/SC29/WG11 w17766, Slovenia*, 2018.
- [44] G. Meynet, Y. Nehmé, J. Digne, and G. Lavoué, "PCQM: A full-reference quality metric for colored 3D point clouds," in *Proc. Int. Conf. Qual. Multimed. Exp. (QoMEX)*, 2020.
- [45] K. He, X. Zhang, S. Ren, and J. Sun, "Deep residual learning for image recognition," in *Proc. IEEE Comput. Soc. Conf. Comput. Vision Pattern Recognit. (CVPR)*, 2016, pp. 770–778.
- [46] V. Sitzmann, J. Martel, A. Bergman, D. Lindell, and G. Wetzstein, "Implicit neural representations with periodic activation functions," in *Proc. Adv. Neural Inf. Process. Syst. (NeurIPS)*, 2020, pp. 7462–7473.
- [47] T.-Y. Lin, P. Goyal, R. Girshick, K. He, and P. Dollár, "Focal loss for dense object detection," in *Proc. IEEE Int. Conf. Comput. Vision (ICCV)*, 2017, pp. 2980–2988.
- [48] F. Draxler, K. Veschgini, M. Salmhofer, and F. Hamprecht, "Essentially no barriers in neural network energy landscape," in *Proc. Int. Conf. Mach. Learn. (ICML)*, 2018, pp. 1309–1318.
- [49] T. Garipov, P. Izmailov, D. Podoprikin, D. P. Vetrov, and A. G. Wilson, "Loss surfaces, mode connectivity, and fast ensembling of DNNs," in *Proc. Adv. Neural Inf. Process. Syst. (NeurIPS)*, 2018, pp. 8789–8798.
- [50] E. d'Eon, B. Harrison, T. Myers, and P. A. Chou, "8i voxelized full bodies—a voxelized point cloud dataset," *ISO/IEC JTC1/SC29 Joint WG11/WG1 (MPEG/JPEG) input document WG11M40059/WG1M74006*, vol. 7, no. 8, p. 11, 2017.
- [51] S. Wiedemann, H. Kirchhoffer, S. Matlage, P. Haase, A. Marban, T. Marinč, D. Neumann, T. Nguyen, H. Schwarz, T. Wiegand *et al.*, "DeepCABAC: A universal compression algorithm for deep neural networks," *IEEE J. Sel. Top. Signal Process.*, vol. 14, no. 4, pp. 700–714, 2020.
- [52] MPEGGroup. MPEG-PCC-TMC13. Accessed: 2024. [Online]. Available: <https://github.com/MPEGGroup/mpeg-pcc-tmc13>
- [53] ——. MPEG-PCC-TMC2. Accessed: 2024. [Online]. Available: <https://github.com/MPEGGroup/mpeg-pcc-tmc2>
- [54] G. Bjontegaard, "Calculation of average PSNR differences between RD-curves," *ITU-T SG16 Q*, vol. 6, 2001.